

Full length article

Mechanism of hardening and damage initiation in oxygen embrittlement of body-centred-cubic niobium

Ping-Jiong Yang^{a,1}, Qing-Jie Li^{b,1}, Tomohito Tsuru^{c,d,1}, Shigenobu Ogata^{d,e},
Jie-Wen Zhang^a, Hong-Wei Sheng^f, Zhi-Wei Shan^a, Gang Sha^g, Wei-Zhong Han^{a,*},
Ju Li^{a,h,**}, Evan Ma^{a,b,***}

^a Center for Advancing Materials Performance from the Nanoscale (CAMP-Nano), State Key Laboratory for Mechanical Behavior of Materials, Xi'an Jiaotong University, Xi'an, 710049, China

^b Department of Materials Science and Engineering, Johns Hopkins University, Baltimore, MD, 21218, United States

^c Nuclear Science and Engineering Center, Japan Atomic Energy Agency, 2-4 Shirakata, Tokai-mura, Ibaraki, 319-1195, Japan

^d Department of Mechanical Science and Bioengineering, Osaka University, Osaka, 560-8531, Japan

^e Center for Elements Strategy Initiative for Structural Materials, Kyoto University, Kyoto, 606-8501, Japan

^f School of Physics, Astronomy and Computational Science, George Mason University, Fairfax, VA, 22030, United States

^g Herbert Gleiter Institute of Nanoscience, Nanjing University of Science and Technology, Nanjing, 210094, China

^h Department of Nuclear Science and Engineering and Department of Materials Science and Engineering, Massachusetts Institute of Technology, Cambridge, MA, 02139, United States

ARTICLE INFO

Article history:

Received 4 January 2019

Received in revised form

15 February 2019

Accepted 18 February 2019

Available online 21 February 2019

Keywords:

Niobium

Oxygen embrittlement

Strain hardening

Screw dislocations

V-O complex

ABSTRACT

Body-centred-cubic metallic materials, such as niobium (Nb) and other refractory metals, are prone to embrittlement due to low levels of oxygen solutes. The mechanisms responsible for the oxygen-induced rampant hardening and damage are unclear. Here we illustrate that screw dislocations moving through a random repulsive force field imposed by impurity oxygen interstitials readily form cross-kinks and emit excess vacancies in Nb. The vacancies bind strongly with oxygen and screw dislocation in a three-body fashion, rendering dislocation motion difficult and hence pronounced dislocation storage and hardening. While self-interstitials anneal out fast during plastic flow, the vacancy-oxygen complexes are stable against passing dislocations. The debris in fact amplify the random force field, facilitating the generation of even more defects in a self-reinforcing loop. This leads to unusually high strain hardening rates and fast breeding of nano-cavities that underlie damage and failure.

© 2019 Acta Materialia Inc. Published by Elsevier Ltd. All rights reserved.

1. Introduction

Metals can dissipate a great deal of mechanical energy via plastic deformation, before damage is accumulated inside to cause dramatic change in the component topology, i.e., fracture. While

the ultimate damage is in the form of high-aspect-ratio planar cracking [1], the initial microscopic damage arises from cavitation, i.e., formation of voids and cavities. Gases such as H₂, O₂, and helium are well known to accelerate the damage initiation in metals and alloys, sometimes in mysterious ways.

Refractory body-centred-cubic (BCC) metals are widely used in nuclear energy, heating elements and rockets [2,3] due to their high melting temperature, excellent strength and creep resistance and good compatibility with liquid metals. However, their mechanical properties rapidly degrade in the presence of dilute impurities such as O, C and N [4–10]. Niobium (Nb), for instance, has appreciable oxygen solubility, and hardens and embrittles at low oxygen levels, decreasing its malleability and fracture toughness and limiting its applications [3–6]. The mechanism that mediate the hardening and embrittlement is the subject of this study.

Oxygen readily enters Nb as impurity in octahedral interstices

* Corresponding author. Center for Advancing Materials Performance from the Nanoscale (CAMP-Nano), State Key Laboratory for Mechanical Behavior of Materials, Xi'an Jiaotong University, Xi'an, 710049, China.

** Corresponding author. Department of Nuclear Science and Department of Materials Science and Engineering, Massachusetts Institute of Technology, Cambridge, MA, 02139, United States.

*** Corresponding author. Department of Materials Science and Engineering, Johns Hopkins University, Baltimore, MD, 21218, United States.

E-mail addresses: wzhanxjtu@mail.xjtu.edu.cn (W.-Z. Han), liju@mit.edu (J. Li), ema@jhu.edu (E. Ma).

¹ These authors contribute equally to this work.

during processing or service [3–6]. The solid solution strengthening effect is traditionally attributed to the attractive interactions between the solute atoms and the dislocation core [11–18]. However, in the following we will show that the two-body interaction between oxygen and screw dislocation (SD) core in Nb is repulsive (also observed for other group V metals and their alloys), and the hardening likely involves unconventional factors. Previous studies of BCC metals indicate that the motion of screw dislocations (SDs) under high stresses can generate excess vacancies [19–24]. Here by “excess”, we mean well beyond the thermal equilibrium concentration. We will show in the following that the presence of oxygen can play a role in the generation and stabilization of vacancies, and these metal-vacancy clusters can interfere with running dislocations to cause hardening and also mediate damage accumulation. This results in accelerated hardening and embrittlement, as discussed below. Because damage develops on multiple time and length scales, beyond the detection ability of a single method, our study combines experimental microstructure analysis underneath the bulk fracture surface, nanoscale mechanical testing, and atomistic computational modeling.

2. Experimental and simulation method

2.1. Preparation of Nb-O solid solution

Heat treatment of nominally pure Nb (with 140 wppm O, 57 wppm N and 88 wppm C) was carried out in a tube furnace, evacuated to a pressure of ~ 250 Pa and then heated to 1000°C and held for 1 h, followed by furnace cooling. Oxygen and nitrogen remaining in the furnace were absorbed by the Nb samples. After the heat treatment the sample was mechanically polished to remove the surface oxide. The resultant Nb-O sample contained 1800 wppm O, 120 wppm N and 78 wppm C, as measured using a LECO ONH836 Oxygen/Nitrogen/Hydrogen Elemental Analyzer and a LECO CS844 Carbon/Sulfur analyzer. Similar methods were used to prepare bulk tensile samples and Nb-O single crystal pieces.

2.2. Bulk and micro-scale tensile test

Polycrystalline Nb with average grain size of $\sim 70\ \mu\text{m}$ was cut into dog-bone specimen with the dimensions of 12 mm (length) \times 5 mm (width) \times 0.5 mm (thickness), via wire cutting. After cleaning in acetone, the sample was put into the tube furnace for oxygen charging (section 2.1). Bulk tensile tests were conducted at a strain rate of $1 \times 10^{-3}\ \text{s}^{-1}$ on a MTS tensile machine for both Nb and Nb-O polycrystalline samples. In order to check the effect of different oxygen concentration on the tensile properties of Nb, we also performed the oxygen charging at 500°C , 600°C , 700°C and 800°C for 1 h (Fig. S1). At least five samples were tested for each group.

Single crystal Nb disk was sliced into rectangular plates with dimension of 2 mm \times 3 mm \times 0.5 mm by wire cutting. After cleaning in acetone, the samples were put into the tube furnace to produce Nb-O samples. Then the sample was mechanically ground down from one side to the final thickness of $\sim 40\ \mu\text{m}$ while the other surface adhered to the polishing tool to ensure the crystal orientation. The micro-tensile samples were milled by using focused ion beam (FIB). Firstly, a thin plate with 5 μm (length) \times 2.5 μm (width) \times 800 nm (thickness) was FIBed from the bulk sample. Then a dog-bone like structure with dimensions of 1 μm (length) \times 400 nm (width) \times 800 nm (thickness) was micro-machined. Finally, the sample was thinned down to the desired thickness of 150 nm from two sides of the sample by using a low ion beam current to minimize the Ga⁺ damage. *In-situ* mechanical tests were conducted using a Hysitron PI95 TEM PicoIndenter inside a

JEOL 2100F TEM (200 KV) under displacement control. The displacement rate was programmed to be 5 nm/s, corresponding to a strain rate of $\sim 5 \times 10^{-3}\ \text{s}^{-1}$. More than 4 tests were conducted for each loading orientation. The size and loading axis of all the single-crystal Nb-O microsamples were determined in SEM and TEM before each tensile test.

2.3. DFT calculations

We firstly constructed atomic models of dislocation core structure. The introduction of dislocation dipole in a periodic cell is accomplished through application of a continuum linear elastic theory solution for the periodic dislocation dipole array [25]. Lattice constant a_0 and elastic constants C_{11} , C_{12} and C_{44} for Nb, needed to solve the elastic problem of dislocation dipole, are $a_0 = 3.323\ \text{\AA}$, $C_{11} = 247.4\ \text{GPa}$, $C_{12} = 139.0$ and $C_{44} = 16.5\ \text{GPa}$. The distortion field is then chosen to minimize the total elastic energy subject to the topological constraints imposed by the dislocations. The predicted displacement at the atomic positions is obtained by a line integral starting from a reference coordinate. In this work, the $\langle 111 \rangle$ screw dislocation dipole is considered. The dipole is inserted into a 405 atom supercell with three layers along $\langle 111 \rangle$ direction. Subsequently, a vacancy and oxygen interstitial were inserted around dislocation core.

We then carried out the density functional theory (DFT) calculations to obtain stable configuration of dislocation core around an oxygen interstitial and a vacancy, and investigated the interaction energy between these defects. The DFT calculations were implemented using the Vienna Ab initio simulation package (VASP) [26,27] with the Perdew–Burke–Ernzerhof formulation of the generalized gradient approximation to the exchange-correlation density functional [28]. The plane-wave energy cutoff was set at 400 eV. The Brillouin-zone k-point samplings were chosen using the Monkhorst–Pack algorithm [29]. $1 \times 1 \times 6$ k-point sampling was used for all calculations. Convergence of self-consistent field calculations was determined when energy difference becomes below 10^{-5} eV. The fully relaxed configurations were obtained by the conjugate gradient method that terminated the search when force on all the atoms was reduced to less than 0.01 eV/Å. The transition state during dislocation motion was calculated by nudged elastic band (NEB) method [30]. Nine intermediate replica images were used for NEB simulation and the convergence condition of forces were less than 0.02–0.025 eV/Å. Atomic model used in the present study was visualized by ATOMEYE [31] and VESTA [32] software.

2.4. MD simulations

All the MD simulations are based on our newly developed embedded atom method (EAM) potential for the Nb-O system. The details of EAM potential development and validation will be presented elsewhere. We considered the $\frac{1}{2}\langle 111 \rangle$ screw dislocation which, on average, glides on the {112} plane at 300 K, as predicted by the new EAM potential. For the general purpose of simulating screw dislocation motion, we used a simulation box with dimensions of 23 nm \times 18 nm \times 61 nm along $X[\bar{1}01]$, $Y[1\bar{2}1]$ and $Z[111]$, respectively. Periodic boundary conditions were applied in the dislocation motion direction (i.e., $X[\bar{1}01]$) while free surfaces were used in the other directions. Screw dislocations were introduced according to the anisotropic elasticity theory of dislocation [33] and the corresponding displacement was solved using the Atoms package [34]. For simulations involving various point defects, we introduced the point defects in a random way. For example, vacancies were introduced by randomly removing atoms and oxygen interstitials were introduced on randomly chosen

octahedral sites (both DFT and the EAM potential predict that the octahedral O interstitial is more stable than the tetrahedral O interstitial). In addition to the random sites, V-O defects (i.e., the binding of one O and one vacancy) were also introduced with random orientations regarding the slip plane. All samples were first relaxed at 300 K for 100 ps and then shear was applied either under a constant strain-rate of $5 \times 10^7 \text{ s}^{-1}$ or constant shear stresses to drive the motion of screw dislocation. An integration time step of 1 fs was used to update atomic positions. All simulations were carried out using the LAMMPS package [35] and analyzed by common neighbour analysis [36,37] as implemented in the OVITO package [38].

3. Results

3.1. Solute oxygen induced brittle fracture in tensile test

The experimental samples start with two types of polycrystalline Nb; one is nominally pure Nb with 140 wppm oxygen (hereafter referred to as “Nb”), and the other is Nb with oxygen purposely added to 1800 wppm (i.e., ~1 at% O, hereafter referred to as “Nb-O”, prepared by heating the nominally pure Nb at 1000 °C for 1 h in 250 Pa Ar). Fig. 1(a) demonstrates the observation of oxygen embrittlement, using centimeter-scale bulk tensile tests on these two types of samples. As shown in Fig. 1(a), bulk Nb shows a yield point at ~150 MPa, then strain-hardens slowly to a peak stress of ~200 MPa, and fractures at a total strain of 50%. The inset in Fig. 1(a) shows the final fracture in a shear mode of this ductile Nb sample. In contrast, bulk Nb-O shows more than double the strength, but failed catastrophically, rupturing into several pieces, indicating that the ~1 at% of oxygen solutes drastically hardens and embrittles macroscale Nb. With increasing oxygen concentration, hardening and degradation of ductility becomes more severe in bulk Nb (Fig. S1).

The deformation microstructure underneath the fracture plane (in FIB lift-out samples) was compared for Nb versus Nb-O. In the case of Nb, high density of dislocations and cavities of various sizes are observed a few microns away from the fracture plane, as shown in Fig. S2, indicating profuse plasticity and gradual damage accumulation during necking. In contrast, the Nb-O exhibits transgranular quasi-brittle fracture features at lengthscale of 100 μm , as displayed in Fig. 1(b). Mainly three types of deformation microstructures are formed in local regions near the fracture surface in Nb-O: deformation twins (Fig. 1(c)), slip bands (Fig. 1(g)), and micro-cracks of different aspect ratios beneath the fracture surface (Figs. S3(b) and (c)). These observations indicate that plasticity is more difficult and localized in Nb-O, preceding the crack nucleation and quasi-brittle failure [39,40]. It is difficult to imagine how a metal can separate atomistically at lengthscale of 10^1 nm without coalescence of cavities, but the lengthscale and timescale of such cavity dynamics in bulk Nb-O could be so much smaller and faster than Nb that they are well beyond the range that can be captured in experiments. In other words, there can be a severe space-time “contraction” of the damage progression process. Further microstructural characterizations using Atom Probe Tomography (APT) reconstruction and high-resolution TEM did not detect metal oxides inside the Nb-O (Fig. S4), and the Nb-O atomic distance distribution matches that of a random solid solution (Fig. 1(h) and (i)), thus the embrittlement is mainly caused by the homogeneous distribution of oxygen as solutes.

3.2. Abnormal strain hardening and shear localization

Because damage mechanics is controlled by extreme-value statistics (i.e. the largest flaw is by far the most damaging) [41],

we switched to tensile testing of submicron-sized samples inside a TEM. In this case the total elastic energy is tiny and the lengthscale progression of the plasticity-damage conjugate localization process is interrupted, allowing us to record the flow, hardening and damage accumulation in a small deformation volume. Fig. 2(a) shows a typical example of tensile test of Nb and Nb-O single crystals with [101] orientation. The behavior of Nb is expected: compared with the bulk sample the submicron sample exhibits higher yield strength and frequent strain bursts due to dislocation avalanches [42,43], as shown in Fig. 2(a). Similar to bulk Nb-O, dramatic differences were observed on the stress-strain curve once Nb is oxygenated (Movie S1). The Nb-O single crystal is not only much stronger (yield strength ~1.35 GPa), but also exhibits a rapid strain hardening stage with a near-constant strain hardening rate (Θ) ($\Theta \equiv d\sigma/d\varepsilon$ where σ is the stress and ε is the strain) as high as 12 GPa ($\frac{\Theta}{\mu} \approx 0.32$, where $\mu = 37.5 \text{ GPa}$ is the shear modulus of Nb), far exceeding that for normal metals ($\frac{\Theta}{\mu} < 0.1$) [44–46]. Significant strain hardening was also observed in bulk Nb containing different levels of oxygen (Figs. S1(a) and (b)). After the dramatic strain hardening to peak stress of ~1.9 GPa, pronounced stress drop kicks in as the deformation starts to localize, all the way until the eventual fracture. Similar differences in stress-strain curves and significant strain hardening were also observed for other crystal orientations (Fig. S5).

Supplementary data related to this article can be found at <https://doi.org/10.1016/j.actamat.2019.02.030>.

The small sample size, while known to have significant effect on strength [47], is the same for Nb and Nb-O. Therefore, these prominent differences in the single-crystal plasticity and damage can be attributed to the ~1 at% oxygen solute. Although the overall stress and plastic strain levels are elevated in micro-samples, the local damage initiation process should bear similarity to that of bulk samples. This is because a) the local stress in bulk Nb-O may be close to that in micro-samples due to stress concentration (e.g., 1 GPa local stress can be reached for a minimum stress concentration factor of 3 and a yield stress of 350 MPa in Fig. 1(a)); b) similar stress-strain curves should be expected for micro-scale Nb and Nb-O if high stress is the only cause of damage initiation, which obviously contradicts the experiments; and c) severe localized plasticity was indeed observed for both bulk samples (Fig. 1(g) and Fig. S3) and micro-samples (Fig. 2(d), Figs. S7 and S8).

Unusually large Θ is observed in both bulk and submicron Nb-O samples (Fig. 2(a) and Fig. S1). But the submicron tests give us better temporal control and access to the deformed and/or damaged volume. In order to capture the dislocation structures evolution during the stage of drastic strain hardening, we interrupted the test at the plastic strain of 5% on a [101] submicron-sized Nb-O single crystal (Fig. S6 and Movie S2). A snapshot is shown in Fig. 2(b). As can be seen, very-high-density dislocation substructures are stored in the small-volume sample during the hardening stage, consistent with the extraordinary strain hardening rate observed (Fig. 2(a) and Fig. S5). Such significant dislocation trapping and storage is in contrast to submicron pure metals where most dislocations can be effectively driven out the tiny sample volume [48]. These results indicate that oxygen is effective in pinning down and assisting the storage of dislocations, counteracting the surface sinks.

Supplementary data related to this article can be found at <https://doi.org/10.1016/j.actamat.2019.02.030>.

Different strain localization and fracture behaviors are also observed for submicron Nb and Nb-O samples. The fracture in [101] oriented Nb-O is clearly due to the intense localized slip in a very narrow channel (along both {110} and {112} planes in Fig. S7); incipient crack nucleates at the sample edge intersecting with the localized slip zone, causing catastrophic cleavage fracture along the

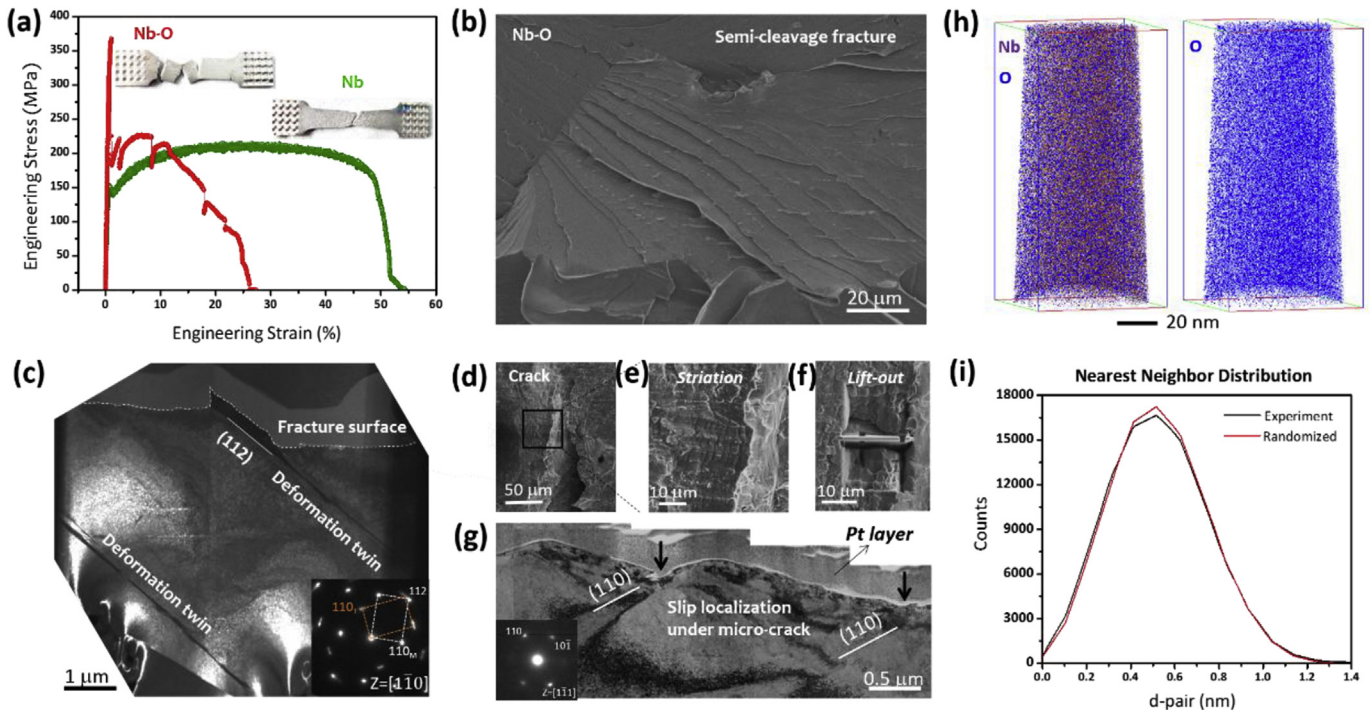


Fig. 1. Bulk tensile test and microstructure under fracture surface. (a) Engineering stress-strain curve of bulk tensile test for Nb (green curve) and Nb-O (red curve). Insets are images of bulk Nb-O and Nb samples after fracture. (b) A typical SEM image of transgranular semi-cleavage fracture surface of the Nb-O sample. (c) A dark field TEM image of deformation twin beneath the ridges of Nb-O fracture surface. The zone axis is $[1\bar{1}0]$. (d) Low-magnification SEM image of the crack tip. (e) High-magnification SEM image of ribbon structures formed near the crack tip in the boxed region in (d). (f) A SEM image showing the position on the fracture surface for cutting the TEM thin foil for further characterization. (g) A bright-field TEM image of the microstructure beneath the ribbon morphology. Distinct localized slip on (110) planes is observed beneath the surface steps, which are indicated by arrows. (h) and (i) Three-dimensional APT reconstruction of the Nb-O sample, showing homogeneous distribution of O in Nb. (For interpretation of the references to color in this figure legend, the reader is referred to the Web version of this article.)

plane 90° to the tensile stress direction (Figs. S7 and S8 and Movie S1, (101) is a low energy plane, thus both Nb and Nb-O show similar cleavage fracture but different strain localization processes). A more prominent difference in fracture behavior is found for the submicron $[001]$ oriented Nb and Nb-O with a thickness of ~ 60 nm. While the failure of Nb is mainly due to necking down caused by intense dislocation slip forming a needle-sharp fracture front (Fig. 2(c)), the fracture of Nb-O is caused by severe slip localization (similar to Fig. 1(g) and Fig. S3(d)) and the ensuing formation and coalescence of oblate nano-cavities (local lighter contrast, as marked by V) with diameter of a few nanometers in one major shear band (Fig. 2(d) and (e)). Detailed deformation process can be visualized in Movies S3 and S4. These results again demonstrate the significant influence of oxygen on the deformation and damage processes leading up to fracture.

Supplementary data related to this article can be found at <https://doi.org/10.1016/j.actamat.2019.02.030>.

4. Modeling to explain the hardening and embrittlement

4.1. Interaction among vacancy, oxygen interstitial and screw dislocation core

We now look into the atomistic origin of the observations above, focusing on the mechanisms of rapid strain hardening and damage accumulation, which can be technically defined as the loss of total metal-metal coordination (TMMC) in a volume. DFT calculations are employed to obtain the two-body and three-body interaction energies among SD, vacancy (V) and oxygen (O) (Fig. 3 and Fig. S9). The two-body interaction energies were calculated for V-O, SD-V, and SD-O. As summarized in Fig. 3(b) and Table 1, the strongest

interaction between a vacancy and an oxygen in BCC Nb was found to be -0.80 eV, associated with the first nearest-neighbour (NN) configuration (Fig. 3(a) and Fig. S9), indicating a strong V-O attraction. For interactions between V and SD, attractive interactions were found: the interaction energies for the first, second and third NN configurations (Fig. S9) are -0.51 eV, -0.49 eV and -0.051 eV, respectively. However, this attractive interaction between a vacancy and a SD decays rapidly with distance. Oxygen, on the other hand, has repulsive interaction with the SD: when an O was placed at the n th NN from the dislocation core, strong repulsive interactions were found up to the fourth NN (see Fig. S9), e.g., the interaction energies for the first, second, third and fourth NN configurations are all positive, 0.34 eV, 0.1 eV, 0.55 eV and 0.54 eV, respectively. In contrast, the three-body interactions between V-O pair and SD core (Fig. 3(b) and Fig. S9) are extremely attractive (Table 2), with an interaction energy of at least -1.0 eV, which exceeds by far the V-SD interaction. In other words, it is the V-O-SD three-body interaction that stands out, potentially responsible for trapping SDs. Note that the interaction energies between solute and a screw dislocation include both the elastic interaction and chemical effects [49].

The resultant dramatic hindrance on SD motion is further demonstrated by nudged elastic band (NEB) calculations [50] on the migration energy of a SD in pure Nb and Nb-O. As shown in Fig. 3(c) and (d), the energy barrier for dislocation motion around the V-O pair is almost an order of magnitude higher than that without V-O pair (0.169 eV/b versus 0.018 eV/b). In addition, we also evaluated the interactions between V_mO_n cluster and SD, as shown in Fig. S10: the formation energy of V_mO_n is reduced significantly when attached to SD. These pronounced three-body interactions and vacancy cluster stabilization may play an

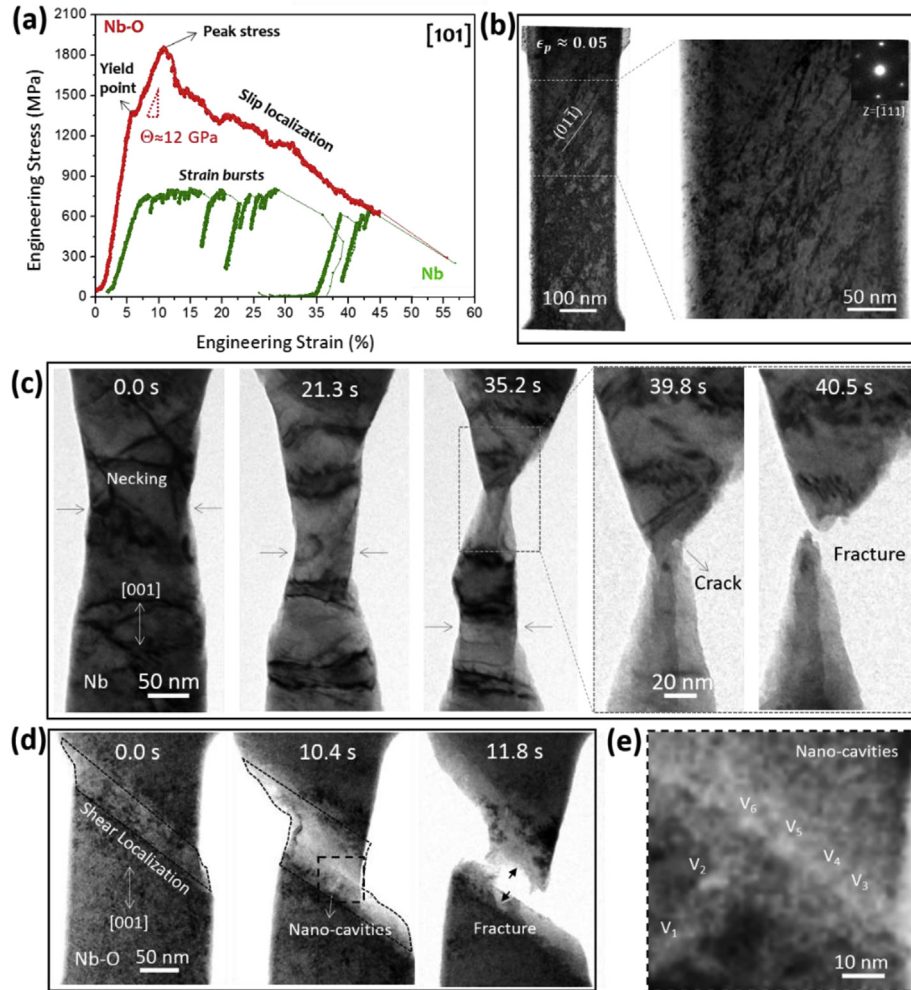


Fig. 2. Nanomechanical tensile tests of submicron-sized Nb and Nb-O inside TEM. (a) The engineering stress-strain curve of Nb (green curve) and Nb-O (red curve) single crystals with loading axis along [101]. (b) A bright-field TEM image showing dislocation storage after unloading at $\sim 5\%$ plastic strain (in the strain hardening stage) for [101] oriented Nb-O. The zone axis is $\bar{1}11$. (c) The necking and fracture behavior of [001] Nb with thickness of ~ 60 nm. (d) Slip localization leading to fracture of [001] Nb-O with thickness of ~ 60 nm: slip localization, nano-cavities formation, and fracture. (e) Close-up view of the nano-cavities formed in (d) marked by black dash square. The larger nano-cavities are labeled by V in (e) (V_1 to V_6 are all formed in the same shear band, which appeared wide because of the projection view at an angle with respect to the e-beam). (For interpretation of the references to color in this figure legend, the reader is referred to the Web version of this article.)

important role in damage initiation of oxygen embrittlement; note that the atomistic processes are beyond the detection limits of current experimental techniques.

4.2. Oxygen solutes enhance cross kink formation and hardening

Rapid hardening arising from the V-O-SD attractive interaction and the formation of oxygen stabilized vacancy clusters require the availability of vacancies. One vacancy introduces $\Delta TMMC = -8$, and is the smallest form of damage. It is well-known that excess vacancies can be created in metals with the injection of plastic work [30,51]. We illustrate next how excess vacancies are efficiently generated and stabilized in the wake of passing SDs. To this end, MD simulations are carried out. Previous experiments and MD studies [19–24] have shown that superabundant vacancies and interstitials can be created in pure BCC metals by pinching off cross-kinks on SDs moving under very high stresses (also see Fig. S11 in the case of pure Nb). The relatively high stress level for SD to generate point-defect in pure Nb is due to the fact that an elevated kink-pair nucleation rate is required for forming and pinching off cross-kinks. Considering the relatively low stress level in our

experiments, that specific mechanism is unlikely to play a dominant role here. However, a new mechanism emerges due to the presence of oxygen. We found that when a SD passes through the O interstitials, the medium-ranged repulsive interactions between the SD and randomly distributed O interstitials constantly twist local dislocation segments onto different glide planes to form cross-kinks, as schematically illustrated in Fig. 4(a). When a SD moves (t_0) through the repulsive random force field (RFF) imposed by O, local segments can be subjected to net forces with different directions (t_1), therefore pushing the local segments onto different glide planes to form cross-kinks (t_2). The local segments then continue to bypass the O solutes via nucleating extra cross-kinks (t_3) that lead the entire dislocation line back to the original glide plane, forming a point defect (t_4). Such a process to “pinch off” point defects is similar to that described in Ref. [20]; however, the required high cross-kink nucleation rate is now driven by the O-RFF, rather than the ultra-high applied stress.

To demonstrate the effects of RFF on gliding SDs, we carried out MD simulations on a single $1/2\langle 111 \rangle$ SD in samples of pure Nb, Nb-O(0.5 at%) and Nb-O(1.0 at%). The introduced SD glides on a $\{112\}$ plane (the predicted glide plane of the current potential at 300 K)

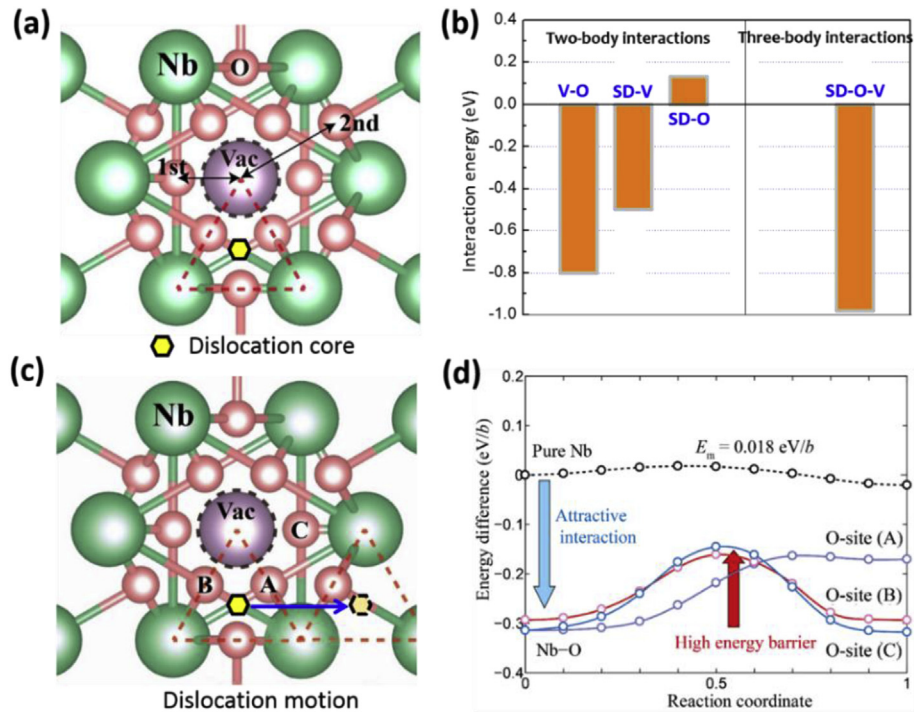


Fig. 3. First-principles calculations of the interaction energy among vacancy, oxygen interstitial and screw dislocation core and the migration energy barrier for screw dislocation in Nb-O. (a) The atomic model of a SD core with a vacancy after inserting an oxygen interstitial. (b) The interaction energy for vacancy-oxygen, vacancy-SD, SD-oxygen and the three-body interaction. (c) The atomic model for the migration motion of SD around a vacancy-oxygen complex. (d) The migration energy of a SD in Nb with and without vacancy-oxygen complex.

Table 1
Two-body interaction energies (including both elastic and chemical effects) among V, O and SD in the unit of eV.

	0 th NN	1 st NN	2 nd NN	3 rd NN	4 th NN
V-O	0.044 ^a	-0.80	-0.17	0.13	-
SD-V	-	-0.51	-0.49	-0.05	-
SD-O	1.75 ^b	0.34	0.10	0.58	0.54

^a Equivalent to the formation energy of substitutional O.

^b Equivalent to an unstable site at the center of SD core.

Table 2
Three-body interaction energies (including both elastic and chemical effects) between V-O pair and SD in the unit of eV.

	O (site1)	O (site2)	O (site3)
V (site0)	-0.94	-0.97	-0.97
V (site1)	-0.95	-1.02	-1.04

and periodic boundary conditions are only applied along the motion direction. All three samples are sheared with a constant strain rate $5 \times 10^7 \text{ s}^{-1}$ at 300 K. As shown in Fig. 4(b), the yielding stress and flow stresses of oxygenated samples are obviously higher than that of the pure Nb sample, suggesting significant hardening effects. Such hardening is due to two factors: a) the RFF induces cross-kinks, requiring higher pinch-off stress (as indicated by the higher yielding point) to maintain SD motion; b) the formation of vacancy-oxygen complex also traps SD during motion. Fig. 4(c) further compares the SD configurations at a shear strain of $\sim 7.3\%$ for samples of pure Nb and Nb-O(0.5 at%), respectively. As expected, the SD glides smoothly in pure Nb sample (the upper panel of Fig. 4(c)) and leaves no point defects behind. In contrast, the SD gliding in the sample of Nb-O(0.5 at%) generates various defects

such as V-O cluster (marked by yellow atoms), vacancies (marked by blue atoms) and vacancy tube (marked by magenta atoms). Note that the stress levels to generate these various defects in Nb-O samples are much lower (~ 0.5 GPa, Fig. 4(b)) than that required in pure Nb (~ 2.5 GPa, see Fig. S11), easily reachable in bulk- and micro-scale experiments. These results emphasize the important role played by the O-RFF in both hardening and defect generation.

The RFF-enhanced cross-kink and point defect formation are expected to work for SDs gliding on both $\{110\}$ and $\{112\}$ planes, as on both types of planes, neither crystallographic restrictions on cross-kink formation nor significant anisotropy of RFF has been found. To demonstrate this, the enhanced cross-kink formation process in action has been studied in detail. We have conducted a finite-temperature ($T = 300$ K) MD simulation of a screw dislocation (Fig. 5(a)–(c)), dislocation core atoms are colored according to their positions along the normal direction of the slip plane, i.e., blue/red atoms are below/above the original slip plane) moving through 0.5 at.% O (easier visualization than the more O-crowded 1 at.% O case) interstitials (smaller blue atoms). As can be seen, once the screw dislocation is subjected to constant rate ($5 \times 10^7 \text{ s}^{-1}$) shear, local segments readily glide onto different slip planes and form cross-kinks (marked using the blue arrows). Such enhanced formation of cross-kinks has not been observed in O-free sample sheared under the same conditions, indicating that O interstitials and the associated RFF are the direct cause of the prominent cross-kink formation. To further verify that the O-RFF can indeed facilitate cross-kink formation, Fig. 5(d) introduces a screw dislocation in a better-defined O force field where the dislocation line is divided into two equal segments and then subjected to opposite repulsive forces imposed by O atoms. In this set-up, the left segment tends to glide downward and the right segment tends to glide upward. Cross-kinks are then expected to form at the joint of the two segments. As seen in Fig. 5(e), after the initial energy

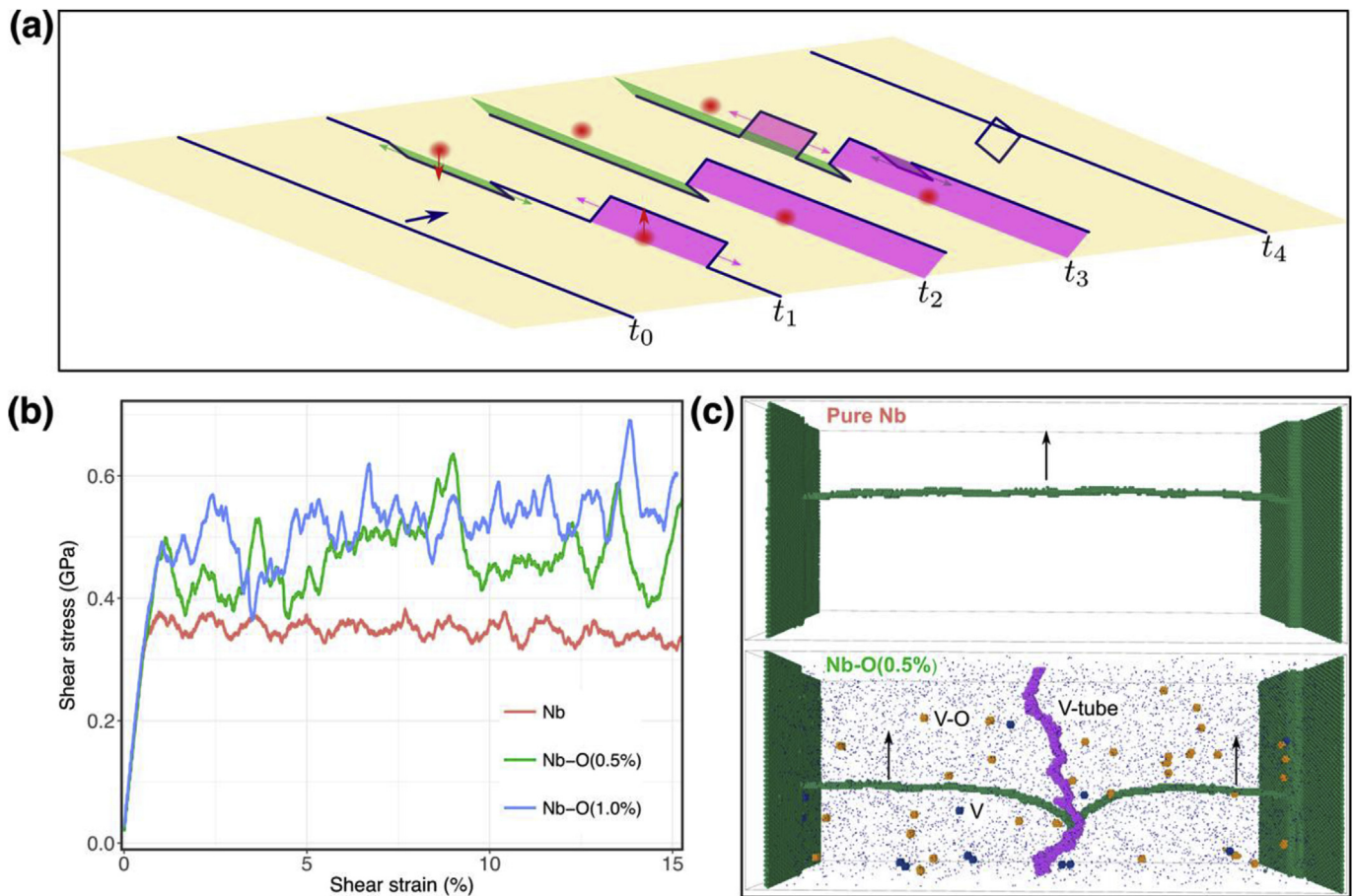


Fig. 4. Random force field (RFF) imposed by O on screw dislocation leads to enhanced cross-kink and point defects formation and hardening. (a) Schematic of cross-kink and point defect formation due to repulsive force field imposed by oxygen solutes. Red arrows indicate the directions of the local repulsive forces. Dislocation segments and kinks are represented by blue lines. The slip plane ($\{112\}$ plane in this case) is rendered in yellow. (b) Shear stress vs. shear strain curves for a single SD gliding in samples of pure Nb, Nb-O(0.5 at.%) and Nb-O(1.0 at.%), respectively. (c) Comparison of SD configurations in pure Nb (upper panel) and Nb-O(0.5 at.%) (lower panel) at a shear strain of $\sim 7.3\%$. Arrows indicate the motion direction of SD. Vacancies, V-O clusters and vacancy tube are marked by blue atoms, yellow atoms and magenta atoms, respectively. SD and free surfaces are marked by green atoms. The SD length is 57 nm. Note that our EAM potential was fitted to the total interactions between solute and screw dislocation from *ab initio* calculations, thus capturing both the elastic and chemical effects. Periodic boundary conditions are only applied in the dislocation motion direction. Free surfaces along the dislocation line direction are adopted to be consistent with grain boundaries and free surfaces in lab experiments and to eliminate artificial cross-kinks resulting from using periodic boundary conditions. Note that free surfaces do not artificially act as kink sources, as indicated by the slight bow-out shape of the dislocation line shown in (c). (For interpretation of the references to color in this figure legend, the reader is referred to the Web version of this article.)

minimization and MD relaxation at 300 K for 10 ps, the left segment and the right segment indeed relocate their positions, i.e., while some local regions of the left segment move slightly downward, the right segment moves entirely upward (the atom colors are mostly red), forming a cross-kink at the joint (indicated by the arrow). Upon shear straining (Fig. 5(f)), the left and right segments glide further downward and upward, respectively, piling up even more cross-kinks at the joint. This set of simulation thus clearly demonstrates that O-RFF enables easy cross-kink formation.

4.3. Atomistic processes of point defect generation

Now let us take a closer look at the atomistic processes of point defect generation, biased stabilization of vacancy and cavity formation. The ensuing pinch-off of cross-kinks generates not only copious vacancies, but also self-interstitials (SI). Fig. 6(a)–(c) show a typical process of ‘instant’ pinch-off, forming a VO-SI pair. As seen, after encountering cross-kinks get pinned by each other in Fig. 6(a), a vacancy immediately takes shape near an O interstitial (Fig. 6(b)). Meanwhile, more cross-kinks are aggregating at the left SI site (Fig. 6(b)). Afterwards both the vacancy and SI are completely

pinched off and the vacancy is captured by an O interstitial, creating a VO-SI pair. Such ‘instant’ pinch-off process not only provides efficient vacancy source but also a strongly coupled generation-stabilization mechanism of vacancies in the O-RFF (otherwise both O and V need to diffuse on a much longer timescale). An even more efficient way to generate various defects is the ‘delayed’ pinch-off process (Fig. 6(d)–(f)). A SI pinning site is formed when cross-kinks block each other and result in a short SI dipole (Fig. 6(d)). However, this SI dipole is not immediately pinched off; instead, a much longer SI dipole (Fig. 6(e)) is dragged out. Eventually, the long SI dipole is pinched off and broken into two separate prismatic loops (Fig. 6(f)). While the SD drags out a long SI dipole on the right side, many individual vacancies and V-O complexes are also formed on the left side (Fig. 6(e)–(f)) via the ‘instant’ pinch-off process. This is because the cross-kinks are often nucleated in pairs; for the halves generating SI the other halves are prone to be instantly pinched off to form vacancies, as vacancy-type point defect is much easier to be closed up. Note that no periodic boundary conditions are applied along the dislocation line direction. Such RFF-enhanced defect generation is analogous to precipitation from a supersaturated solution, i.e., when a SD line is

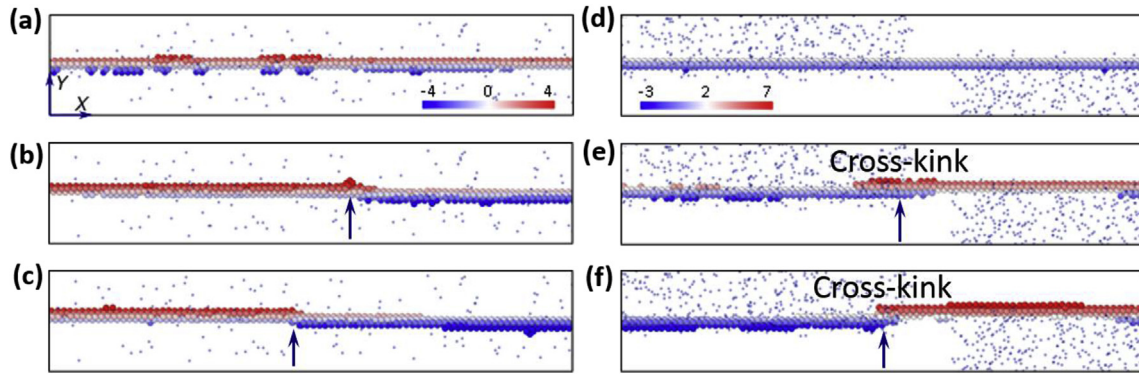


Fig. 5. Cross-kink formation due to repulsive random force field imposed by oxygen solutes. (a–c) MD simulation on cross-kink formation in a 0.5 at.% O (smaller transparent blue atoms) sample. (a), (b), (c) are the snapshots at 90 ps, 115 ps and 190 ps, respectively. Dislocation core atoms are colored according to their positions along the normal direction (i.e., $\langle 112 \rangle$ direction) of the slip plane. Color bar indicates the range of such atomic positions and the unit is Å. Red/blue core means the dislocation segment is above/below the initial position. (d–f) MD simulation on two dislocation segments subjected to relatively uniform opposite forces imposed by O interstitials. (d) is the as-introduced dislocation core. (e) Dislocation segments after the initial energy minimization and MD relaxation at 300 K for 10 ps. (f) Dislocation segments at 168 ps after shear. Arrows indicate the locations where cross-kinks are formed. In all simulations, the applied temperature is 300 K and strain rate is $5 \times 10^7 \text{ s}^{-1}$. X direction is along $\langle 111 \rangle$ and Y direction is along $\langle 112 \rangle$. (For interpretation of the references to color in this figure legend, the reader is referred to the Web version of this article.)

‘saturated’ with cross-kinks created due to external RFF, copious defects of various types are ‘precipitated out’ in its wake so as to maintain the dislocation glide.

4.4. The stability of newly formed SI, V and V-O complex

Notably, the SI, V and V-O complex have very different stability, upon hitting by the passing SD. This creates a sink bias that promotes the accumulation of vacancies ($-\Delta TMMC$) and damage. Fig. 7(a) shows a SD passing through various dynamically formed defects. The SD first reacts with a SI cluster (Fig. 7(b)–(c)); the SI cluster is decomposed into multiple cross-kinks that immediately run away (Fig. 7(c)). In other words, SI can be effectively annealed out to become extra plane of perfect crystal, and new vacancies and V-O complexes are created (Fig. 7(b)–(e)). Similarly, vacancies and weakly bound V-O complexes (O is not in the 1st NN of V) can also be decomposed by moving SD. As shown in Fig. 7(c)–(f), when the SD passes through weakly bound V-O complexes and vacancies, it decomposes all the vacancies into cross-kinks and some of them then ‘precipitate out’ as new vacancies on the left side when meeting other appropriate cross-kinks. In contrast, all V-O

complexes, except for those weakly bound, stay put after the SD passes through (see Fig. 7(f)).

To further confirm the stability of V-O complexes, we performed separate simulations to drive a SD through an array of V-O complexes. As seen in Fig. S12 and Movie S5, almost all the V-O complexes remain stable inside the grain, and some of them even grow into bigger nano-cavities by absorbing excess vacancies created during SD motion. This set of simulation results thus demonstrate very different relative stabilities for SI and V-O complexes, i.e., with the passing of SDs, SI are effectively annealed out but V-O complexes can largely remain *inside* the crystal, creating a strong bias to accumulate nano-cavity damage with larger and larger $-\Delta TMMC$, both in the average and the extreme-value statistics [41] senses. Such interplay between SDs and the dynamically formed defects (V-O complexes, vacancies and SI) highlight an auto-catalyzed, self-reinforced damage accumulation process. Note that all the above processes occur on the displacive timescale rather than on the longer diffusive timescale, therefore effectively pre-empting the diffusive annealing of damage. The stress level required for this mechanism to operate is not high and falls within the range of our experiments.

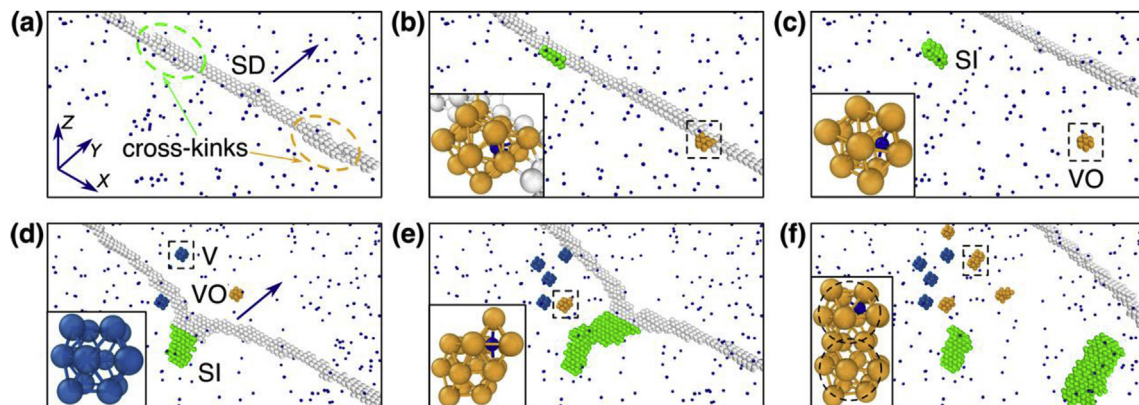


Fig. 6. Cross-kink pinch-off to generate debris. (a) Cross-kinks are formed on a moving SD. (b) A vacancy (surrounded by yellow atoms) starts to form near an oxygen atom (small blue atoms); a SI (surrounded by green atoms) also starts to form. (c) The vacancy is completely pinched off and captured by the O atom, forming a V-O complex (the yellow atom cluster with a blue O atom inside). The SI is also pinched off. (d) A new SI cluster is emerging at a pinning point due to cross-kinks. The inset shows the structure of one vacancy. (e) SD continues to drag out larger SI cluster, generate more vacancies and a new V-O complex. The inset shows the structure of a weakly bound V-O complex as outlined by the dashed rectangle. (f) The SI cluster is completely pinched off and is broken into two individual SI clusters, and more V-O complexes are formed. The inset shows another weakly bound V-O complex (dashed rectangle). (For interpretation of the references to color in this figure legend, the reader is referred to the Web version of this article.)

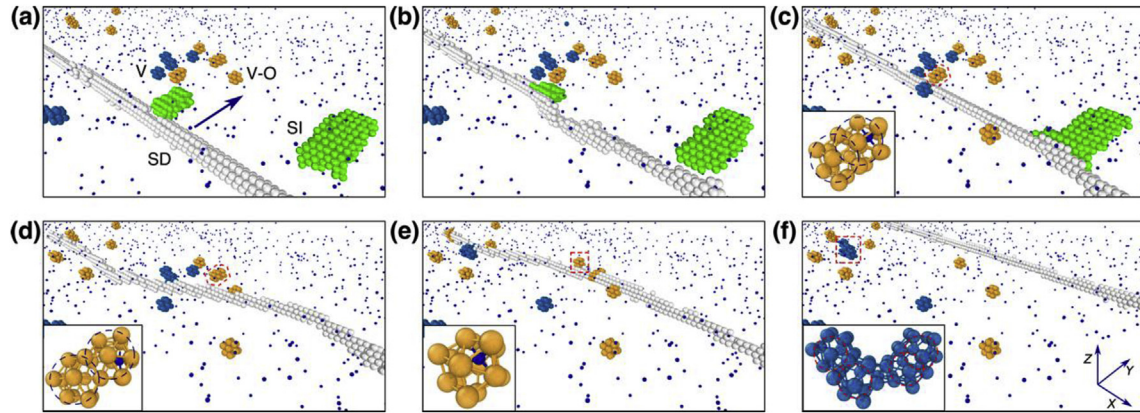


Fig. 7. Self-interstitial, vacancy and V-O complex exhibit different stability when hit by passing screw dislocation. (a) A screw dislocation is gliding towards various dynamically formed defects. (b–c) The screw dislocation decomposes the first SI cluster into cross-kinks and form three new V-O complexes and a vacancy. The inset in (c) shows the structure of a weakly bound V-O complex and a vacancy into cross-kinks. The inset of (d) shows the structure of another weakly bound V-O complex (V_2O_1 , highlighted by the red dashed enclosure), which is decomposed into cross-kinks later. (e) New vacancies are formed on the left-side. The inset of (e) shows a V-O complex (highlighted by the red dashed rectangle) that remains stable after the screw dislocation passes through in (f). (f) The screw dislocation passes through more V-O complexes and most of them remain stable. The inset of (f) shows the vacancy clusters (V_4 , the red dashed rectangle) formed by relocating the vacancies on the right-side in (c) to (e). (For interpretation of the references to color in this figure legend, the reader is referred to the Web version of this article.)

Supplementary data related to this article can be found at <https://doi.org/10.1016/j.actamat.2019.02.030>.

4.5. Damage accumulation to form nano-cavities

Our MD simulations have captured how nano-cavities are nucleated and efficiently grown athermally, even on very short timescale and small lengthscale. As shown in Fig. 8(a) and (b), following the ‘delayed’ pinch-off mechanism, a long V-O tube takes shape as a SD passes through, together with a continuously increasing population of V-O complexes as well as vacancies. Such a much-delayed pinch-off of vacancy debris is generally observed in the modified RFF after some passes of SDs. This is because prismatic loops of vacancy type are generally much easier to be closed up and detached from the SD when compared to SI prismatic loops [20]. However, with increasing passes of SDs in a modified RFF, the probability to create a much more stable atomic jog (e.g., with larger jog height) would be increased such that the ‘instant’ pinch-off forming individual vacancies becomes less likely. The long V-O tube formed generally is quite stable as O are readily available along the tube to stabilize it from collapsing. As a result, later SDs continue the same action along the existing vacancy tube, quickly expanding the cross-section area (the diameter of the tube is ~ 2 nm in Fig. 8(d)) of the V-O tube (Fig. 8(c)–(d)). The individual SD segments can continue to form new V-O tubes near the existing one in a similar way (Fig. 8(d)–(e)). In Fig. 8(e), we take the snapshot after nine passes of SDs to illustrate the large prolate nano-cavities (with sizes from 1 nm to 2 nm) being formed. Fig. 8(f) depicts the cross-section indicated by the two parallel dashed lines in Fig. 8(e) on the tube-shaped nano-cavities, showing a hollow and sheared shape. Fig. 8(g) shows a V-O clusters where vacancies are interconnected and stabilized by O interstitials. With more and more V-O tubes formed near each other, these nano-cavities would eventually coalesce and result in crack initiation (Fig. 2(d) and (e)), in an expected prolate-to-oblate transition, a process driven by elasticity. Detailed damage accumulation process can be found in Movie S6 (0.5 at.% O sample) and Movie S7 (1.0 at.% O sample). There appears to be also “displacive accumulation” of point defects and defect clusters that can happen even at zero temperature, expedited by stress-driven displacive events, unlike typical thermally activated diffusional processes [52,53]. This additional athermal mode of

rapid accumulation of damage will be analyzed elsewhere.

Supplementary data related to this article can be found at <https://doi.org/10.1016/j.actamat.2019.02.030>.

4.6. Oxygen induced embrittlement in Nb

To recapitulate, we have used DFT and MD simulations to discover the mechanisms for hardening and damage initiation on atomic scale. They are not resolvable due to limited temporal and spatial resolution in laboratory experiments. We have uncovered the following “vicious cycle” for damage initiation. The initial repulsive RFF imposed by O interstitials on SDs facilitates the formation of cross-kinks [20] to generate excess defects such as vacancies, V-O complexes and SIs at a low stress (Figs. 4 and 6). Upon the passing of ensuing SDs, SIs can be easily annealed out while most of the V-O complexes remain stable, creating a strong bias for damage accumulation. Nano-cavities are then efficiently formed by the ‘delayed pinch-off’ of vacancy dipoles and stabilized by oxygen interstitials. This displacive damage accumulation mechanism is rapid and highly efficient. These dynamically formed V-O complexes are obstacles for SDs and their average spacing is very small (< 2 nm), and are much more difficult to be “picked up” by the dislocations compared to the SI clusters.

In this context, the dynamically formed oxygen-vacancy complexes pin the moving dislocation. As such, the flow stress (τ) needed for dislocation to bow out in between the neighboring roadblocks is,

$$\tau = \frac{\alpha \mu b}{\lambda} \quad (1)$$

where α is a constant in the range of 0.1–0.5, $\mu = 37.5$ GPa is the shear modulus of Nb, b is the Burgers vector of dislocation, and λ is the average spacing between oxygen-vacancy complexes that each sets a pinning site for the mobile dislocations. The mean free path of the dislocation, L , which is controlled by λ , results in a shear strain of

$$\gamma = \rho b L = b \times \frac{1}{\lambda^2} \times \lambda = \frac{b}{\lambda} \quad (2)$$

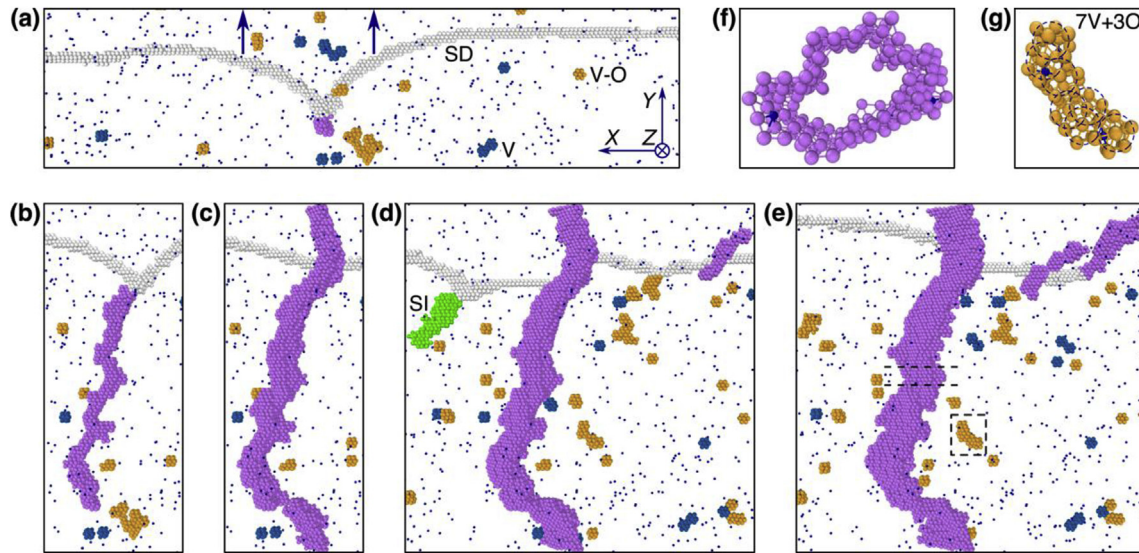


Fig. 8. Damage accumulation to form nano-cavities. (a) A SD is forming a vacancy pinning site (purple atoms). (b) The SD drags out a long V-O tube after the 1st pass of SD. (c) The V-O tube becomes larger as subsequent SDs continue to drag out vacancies on the existing vacancy tube. (d) The size of the V-O tube is significantly increased after six passes of SDs. (e) After nine passes of SDs, more V-O clusters are formed while the existing nano-cavities become even larger. (f) The cross section indicated by the pair of dashed lines on the largest tube-shaped nano-cavities in (e). (g) The structure of a V-O cluster highlighted by the rectangle in (e). (For interpretation of the references to color in this figure legend, the reader is referred to the Web version of this article.)

where ρ is the dislocation density. Therefore, the strain hardening rate can be estimated as [46],

$$\Theta = \frac{d\tau}{d\gamma} = \frac{d\left(\frac{\alpha\mu b}{\lambda}\right)}{d\left(\frac{b}{\lambda}\right)} = \alpha\mu \quad (3)$$

In the extreme case of a homogeneous distribution of the 1 at.% of oxygen atoms in the Nb lattice, their average spacing could be as small as ~ 1.22 nm. Therefore the dynamically formed oxygen-vacancy complexes would make the dislocation glide very difficult, leading to an unprecedented strain hardening rate. Eq. (3) predicts a strain hardening rate in the range of 3.75–18.75 GPa. This magnitude is consistent with the experimental observation displayed in Fig. 2 and Fig. S5. On top of the isotropic strain hardening, a significant kinematic hardening was also observed in Nb-O due to the dynamic formation of oxygen-vacancy complexes, as shown in Fig. S6.

Various dynamically formed defects further randomize the local force field on ensuing SDs, setting the stage for the generation of even more debris, resulting in a self-reinforcing loop. In terms of initiating damage, the biased vacancy accumulation at V-O provides the seed to form nano-cavities that can coalesce (Fig. 2) and precipitously decrease the apparent stiffness of the region due to geometrical softening. The whole process, if embedded in a macroscopic sample with large total stored elastic energy, is highly nonlinear and rapid, giving rise to a dramatic space-time “contraction” effect of the damage accumulation, in which case the damage localization, i.e. inequalities of plastic strain and damage (right after the peak hardening is reached) is extreme and erratic (Fig. 1). If the whole sample however is just of micron-size or smaller, then the total stored elastic energy is smaller and this natural lengthscale progression of the plasticity-damage conjugate localization process is interrupted, and Nb-O appears to strain harden faster and “tougher” than Nb, as the areas under the stress-strain curves in Fig. 2(a) and S5 would suggest.

The damage initiation mechanisms demonstrated above are expected to be general in BCC metals. First, the RFF mechanism underlying the enhanced cross-kink and point defects generation is

expected to be applicable under a wide range of strain rates, from typical laboratory experiment to MD simulations. We carried out extra MD simulations under constant shear stresses to estimate the lower bound of the working range for the random force field. At 300K and a shear stress as low as 0.3 GPa (further lower stress levels would need significantly longer time to observe dislocation motion, which is beyond typical MD simulation timescale), we still observe point defects generation in the Nb-O sample (see Fig. S11(c)). In contrast, point defects are generated in pure Nb sample only when the shear stress is greater than ~ 2.5 GPa (see Fig. S11(a)-(b)). This suggests that the RFF lowers the required shear stress for point defects formation by at least one order of magnitude for the current simulations setup. According to our MD simulations, the mobility of the screw dislocation, at 0.3 GPa in the Nb-O sample, is on the order of 10^{-1} m/s. Then the corresponding strain rate can be approximated using the Orowan equation, $\dot{\gamma} = \rho bv$, where ρ is the mobile dislocation density, b is the magnitude of Burgers vector and v is the dislocation velocity. At high temperatures, the grown-in dislocation density in Nb is roughly $10^{10}/\text{m}^2$ [54]. However, the mobile dislocation density leading to localized slip should be much lower than this. For example, if we consider a typical grain in the bulk sample (the average grain size in our experiment is ~ 70 μm) subjected to localized slip, i.e., a constantly operating dislocation source (e.g., Frank-Read source) emitting one mobile dislocation each time to glide across the grain, then the mobile dislocation density is estimated to be on the order of $10^8/\text{m}^2$. Using this estimated mobile dislocation density and the dislocation velocity (10^{-1} m/s) at 0.3 GPa in MD simulation, we get a strain rate on the order of 10^{-3} s^{-1} , similar to that used in our experiments. This suggests that at a strain rate comparable to that in typical lab experiments, the random force field still significantly enhances the cross-kink and point defect formation. Second, strong interactions between light solutes and SD are common in BCC metals. The resultant random force field of either repulsive (see Fig. S13 for the calculations on other group V BCC metals) or attractive type [55] would significantly enhance cross-kink and point defect generation. Third, it is also commonplace in BCC metals for light elements to stabilize vacancies [56,57]. As these are the key factors involved

in the presented hardening and damage initiation mechanism, the mechanism should be widely active in BCC metals.

5. Conclusion

We have demonstrated and analyzed an example of the general triangular relationship between mobile impurity species, plasticity and damage. This interplay leads to fast hardening and embrittlement of Nb, as seen in our experiments. Our MD simulations reveal that under the repulsive force field due to O solutes, the screw dislocation emits vacancy clusters and interstitial clusters much like in primary radiation damage. O stabilization suppresses the decomposition of vacancies into kinks by passing screw dislocations. The dynamic formation of copious stabilized V-O complexes during plastic deformation strongly obstructs the movement of screw dislocations to cause marked hardening. Meanwhile the 'delayed pinch-off' of cross-kinks accumulate vacancies, which are further stabilized by O interstitials, to instigate damage, and the nano-cavities coalesce to cause failure. While our model case is O in Nb, the defect mechanisms uncovered are likely to be relevant not only to O-embrittlement but also to generic damage problems including irradiation and H-embrittlement, when screw dislocations are important for plasticity such as in BCC materials.

Acknowledgements

W.Z.H. would like to thank the National Key Research and Development Program of China (2017YFB0702301), the National Natural Science Foundation of China (Grant Nos.51471128 and 51621063), the 111 Project of China (Grant No. BP2018008), and the Innovation Project of Shannxi Province (Grant No. 2017KTPT-12). Q.J.L. and E.M. acknowledges the support by US DoE-BES-DMSE, under contract no. DE-FG02-16ER46056. J.L. acknowledges the support by NSF DMR-1410636. T.T. acknowledges JSPS KAKENHI Grant No. 16K06714. S.O. acknowledges the support by the Elements Strategy Initiative for Structural Materials (ESISM) and JSPS KAKENHI Grant No. JP17H01238. All DFT simulations were performed on JAEA ICE X system. We appreciate the help from Prof. D.C. Chrzan and Dr. M. Itakura with ab initio modeling and Prof. C.L. Jia, Prof. S.B. Mi, Dr. L. Lu and Mr. J. Xue in TEM and APT characterization.

Appendix A. Supplementary data

Supplementary data to this article can be found online at <https://doi.org/10.1016/j.actamat.2019.02.030>.

References

- [1] F.R.N. Nabarro, The strains produced by precipitation in alloys, *Proc. Roy. Soc. Lond. A* 175 (1940) 519–538.
- [2] D.R. Trinkle, C. Woodward, The chemistry of deformation: how solutes soften pure metals, *Science* 310 (2005) 1665–1667.
- [3] J.T. Busby, K.J. Leonard, Space fission reactor structural materials: choices past, present, and future, *J. Occup. Med.* 4 (2007) 20–26.
- [4] C.R. Tottle, The physical and mechanical properties of niobium, *Inst. Met.* 85 (1957) 375–378.
- [5] J.R. Donoso, R.E. Reed-Hill, Slow strain-rate embrittlement of niobium by Oxygen, *Metall. Trans. A* 7A (1976) 961–965.
- [6] B.A. Pint, J.R. DiStefano, The role of oxygen uptake and scale formation on the embrittlement of vanadium alloys, *Oxid. Metals* 63 (2005) 33–55.
- [7] J.R. DiStefano, L.D. Chitwood, Oxidation and its effects on the mechanical properties of Nb–1Zr, *J. Nucl. Mater.* 295 (2001) 42–48.
- [8] M.S. El-Genk, J.M. Tournier, A review of refractory metal alloys and mechanically alloyed-oxide dispersion strengthened steels for space nuclear power systems, *J. Nucl. Mater.* 340 (2005) 93–112.
- [9] K.J. Leonard, J.T. Busby, S.J. Zinkle, Influence of thermal and radiation effects on microstructural and mechanical properties of Nb–1Zr, *J. Nucl. Mater.* 414 (2011) 286–302.
- [10] G. Liu, G.J. Zhang, F. Jiang, X.D. Ding, Y.J. Sun, J. Sun, E. Ma, Nanostructured high-strength molybdenum alloys with unprecedented tensile ductility, *Nat. Mater.* 12 (2013) 344–350.
- [11] B.A. Bilby, On the interactions of dislocations and solute atoms, *Proc. Phys. Soc. A* 63 (1950) 191–200.
- [12] N.I. Medvedeva, Y.N. Gornostyrev, A.J. Freeman, Solid solution softening and hardening in the group-V and group-VI bcc transition metals alloys: first principles calculations and atomistic modeling, *Phys. Rev. B* 76 (2007) 212104.
- [13] K. Lu, L. Lu, S. Suresh, Strengthening materials by engineering coherent internal boundaries at the nanoscale, *Science* 324 (2009) 349–352.
- [14] J.F. Nie, Y.M. Zhu, J.Z. Liu, X.Y. Fang, Periodic segregation of solute atoms in fully coherent twin boundaries, *Science* 340 (2013) 957–960.
- [15] Q. Yu, L. Qi, T. Tsuru, R. Traylor, D. Rugg, J.W.M. Jr, M. Asta, D.C. Chrzan, A.M. Minor, Origin of dramatic oxygen solute strengthening effect in titanium, *Science* 347 (2015) 635–639.
- [16] M. Kuzmina, M. Herbig, D. Ponge, S. Sandlobes, D. Raabe, Linear complexes: confined chemical and structural states at dislocations, *Science* 349 (2015) 1080–1083.
- [17] D. Rodney, L. Ventelon, E. Clouet, L. Pizzagalli, F. Willaime, Ab initio modeling of dislocation core properties in metals and semiconductors, *Acta Mater.* 124 (2017) 633–659.
- [18] Y. Zhao, J. Marian, Direct prediction of the solute softening-to-hardening transition in W–Re alloys using stochastic simulations of screw dislocation motion, *Model. Simulat. Mater. Sci. Eng.* 26 (2018), 045002.
- [19] H.J. Kaufmann, A. Luft, D. Schuize, Deformation mechanism and dislocation structure of high-purity molybdenum single crystals at low temperatures, *Cryst. Res. Technol.* 19 (1984) 357–372.
- [20] J. Marian, W. Cai, V.V. Bulatov, Dynamic transitions from smooth to rough to twinning in dislocation motion, *Nat. Mater.* 3 (2004) 158–163.
- [21] A. Dutta, Compressive deformation of Fe nanopillar at high strain rate: modalities of dislocation dynamics, *Acta Mater.* 125 (2017) 219–230.
- [22] A. Stukowski, D. Cereceda, T.D. Swinburne, J. Marian, Thermally-activated non-Schmid glide of screw dislocations in W using atomistically-informed kinetic Monte Carlo simulations, *Int. J. Plast.* 65 (2015) 108–130.
- [23] H.J. Lee, B.D. Wirth, Molecular dynamics simulation of dislocation–void interactions in BCC Mo, *J. Nucl. Mater.* 386 (2009) 115–118.
- [24] J. Chaussidon, M. Fivel, D. Rodney, The glide of screw dislocations in bcc Fe: atomistic static and dynamic simulations, *Acta Mater.* 54 (2006) 3407–3416.
- [25] M.S. Daw, Elasticity effects in electronic structure calculations with periodic boundary conditions, *Comput. Mater. Sci.* 38 (2006) 293–297.
- [26] G. Kresse, J. Hafner, Ab initio molecular dynamics of liquid metals, *Phys. Rev. B* 47 (1993) 558–561.
- [27] G. Kresse, J. Furthmüller, Efficient iterative schemes for ab initio total-energy calculations using a plane-wave basis set, *Phys. Rev. B* 54 (1996) 11169–11186.
- [28] J.P. Perdew, J.A. Chevary, S.H. Vosko, K.A. Jackson, M.R. Pederson, D.J. Singh, C. Fiolhais, Atoms, molecules, solids, and surfaces: applications of the generalized gradient approximation for exchange and correlation, *Phys. Rev. B* 46 (1992) 6671–6687.
- [29] H.J. Monkhorst, J.D. Pack, Special points for Brillouin-zone integrations, *Phys. Rev. B* 13 (1976) 5188–5192.
- [30] H. Mecking, Y. Estrin, The effect of vacancy generation on plastic deformation, *Scripta Metall.* 14 (1980) 815–819.
- [31] J. Li, AtomEye: an efficient atomistic configuration viewer, *Model. Simulat. Mater. Sci. Eng.* 11 (2003) 173.
- [32] K. Momma, F. Izumi, VESTA 3 for three-dimensional visualization of crystal, volumetric and morphology data, *J. Appl. Crystallogr.* 44 (2011) 1272–1276.
- [33] J.P. Hirth, J. Lothe, *Theory of Dislocation*, second ed., Wiley, New York, 1982.
- [34] P. Hirel, Atomsk: a tool for manipulating and converting atomic data files, *Comput. Phys. Commun.* 197 (2015) 212–219.
- [35] S. Plimpton, Fast parallel algorithms for short-range molecular dynamics, *J. Comput. Phys.* 117 (1995) 1–19.
- [36] H. Tsuzuki, P.S. Branicio, J.P. Rino, Structural characterization of deformed crystals by analysis of common atomic neighborhood, *Comput. Phys. Commun.* 177 (2007) 518–523.
- [37] D. Faken, H. Jónsson, Systematic analysis of local atomic structure combined with 3D computer graphics, *Comput. Mater. Sci.* 2 (1994) 279–286.
- [38] A. Stukowski, Visualization and analysis of atomistic simulation data with OVITO—the Open Visualization Tool, *Model. Simulat. Mater. Sci. Eng.* 18 (2010) 15012.
- [39] K. Farrell, P.R.V. Evans, Some observations on mechanical twinning in polycrystalline niobium, *J. Less Common. Met.* 8 (1965) 222–234.
- [40] F. Sorbello, P.E.J. Flewitt, G. Smith, A.C. Crocker, The role of deformation twins in brittle crack propagation in iron–silicon steel, *Acta Mater.* 57 (2009) 2646–2656.
- [41] P.Y. Zhao, J. Li, Y.Z. Wang, Extended defects, ideal strength and actual strengths of finite-sized metallic glasses, *Acta Mater.* 73 (2014) 149–166.
- [42] J.Y. Kim, D.C. Jang, J.R. Greer, Insight into the deformation behavior of niobium single crystals under uniaxial compression and tension at the nanoscale, *Scripta Mater.* 61 (2009) 300–303.
- [43] N. Friedman, A.T. Jennings, G. Tsekenis, J.Y. Kim, M. Tao, J.T. Uhl, J.R. Greer, K.A. Dahmen, Statistics of dislocation slip avalanches in nanosized single crystals show tuned critical behavior predicted by a simple mean field model, *Phys. Rev. Lett.* 109 (2012), 095507.
- [44] T.E. Mitchell, R.A. Foxall, P.B. Hirsch, Work-hardening in niobium single crystals, *Phil. Mag.* 8 (1963) 1895–1920.

- [45] U.F. Kocks, H. Mecking, Physics and phenomenology of strain hardening: the FCC case, *Prog. Mater. Sci.* 48 (2003) 171–273.
- [46] B. Devincere, T. Kubin, Dislocation mean free paths and strain hardening of crystals, *Science* 320 (2008) 1745–1748.
- [47] A.S. Schneider, D. Kaufmann, B.G. Clark, C.P. Frick, P.A. Gruber, R. Mönig, O. Kraft, E. Arzt, Correlation between critical temperature and strength of small-scale bcc pillars, *Phys. Rev. Lett.* 103 (2009) 105501.
- [48] L. Huang, Q.J. Li, Z.W. Shan, J. Li, J. Sun, E. Ma, A new regime for mechanical annealing and strong sample-size strengthening in body centred cubic molybdenum, *Nat. Commun.* 2 (2011) 547.
- [49] B. Lüthi, L. Ventelon, D. Rodney, F. Willaime, Attractive interaction between interstitial solutes and screw dislocations in bcc iron from first principles, *Comput. Mater. Sci.* 148 (2018) 21–26.
- [50] G. Henkelman, B.P. Uberuaga, H. Jónsson, A climbing image nudged elastic band method for finding saddle points and minimum energy paths, *J. Chem. Phys.* 113 (2000) 9901–9904.
- [51] M. Militzer, W.P. Sun, J.J. Jonas, Modelling the effect of deformation-induced vacancies on segregation and precipitation, *Acta Metall. Mater.* 42 (1994) 133–141.
- [52] A. Ishii, J. Li, S. Ogata, "Conjugate channeling" effect in dislocation core diffusion: carbon transport in dislocated BCC iron, *PLoS One* 8 (2013) e60586.
- [53] S.Z. Li, Y.G. Li, Y.C. Lo, T. Neeraj, R. Srinivasan, X.D. Ding, J. Sun, L. Qi, P. Gumbsch, J. Li, The interaction of dislocations and hydrogen-vacancy complexes and its importance for deformation-induced proto nano-voids formation in α -Fe, *Int. J. Plast.* 74 (2015) 175–191.
- [54] P.R.V. Evans, Dislocation etch pit studies in annealed and deformed polycrystalline niobium, *J. Less Common Met.* 6 (1964) 253–265.
- [55] B. Lüthi, L. Ventelon, D. Rodney, F. Willaime, Attractive interaction between interstitial solutes and screw dislocations in bcc iron from first principles, *Comput. Mater. Sci.* 148 (2018) 21–26.
- [56] A. Ramasubramaniam, M. Itakura, E.A. Carter, Interatomic potentials for hydrogen in α -iron based on density functional theory, *Phys. Rev. B* 79 (2009) 174101.
- [57] K. Ohsawa, K. Eguchi, H. Watanabe, M. Yamaguchi, M. Yagi, Configuration and binding energy of multiple hydrogen atoms trapped in monovacancy in bcc transition metals, *Phys. Rev. B* 85 (2012) 094102.

Supplementary Materials for

Mechanism of Hardening and Damage Initiation in Oxygen

Embrittlement of Body-Centred-Cubic Niobium

Ping-Jiong Yang^{1#}, Qing-Jie Li^{2#}, Tomohito Tsuru^{3,4#}, Shigenobu Ogata^{4,5}, Jie-Wen Zhang¹, Hong-Wei Sheng⁶, Zhi-Wei Shan¹, Gang Sha⁷, Wei-Zhong Han^{1*}, Ju Li^{1,8*}, Evan Ma^{1,2*}

The file includes:

Figures S1-S13

Movies S1-S7

Figure S1

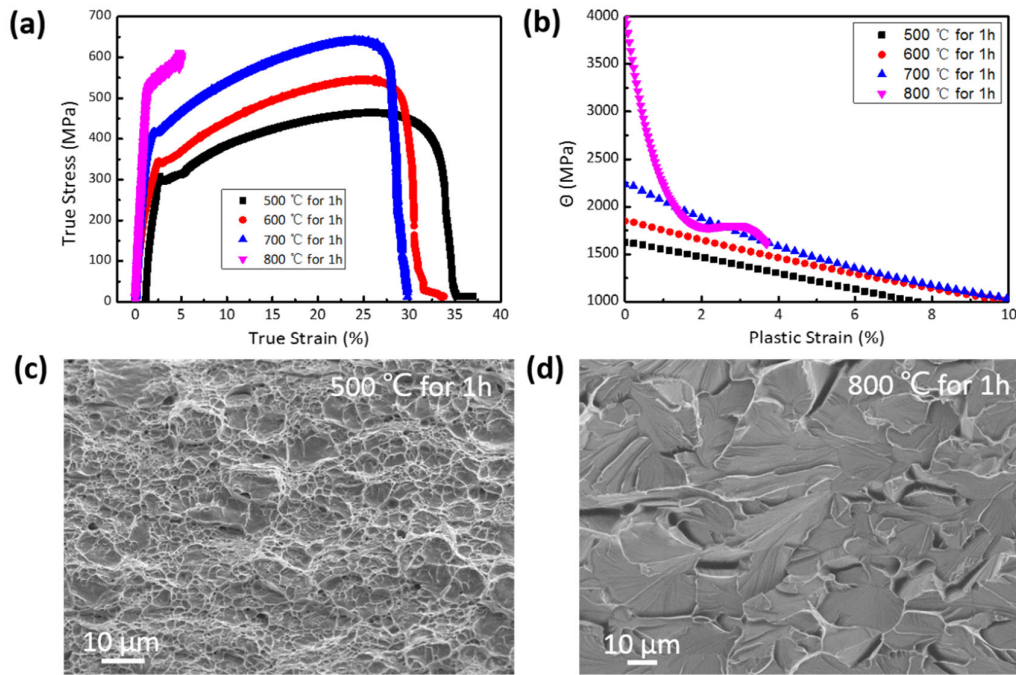


Fig. S1. Bulk tensile tests of Nb after oxygen charging at different temperature. (a) True stress-strain curves of Nb with different oxygen concentration after charging at high temperature (500 to 800 °C). (b) Strain hardening plot of the true stress-strain curves shown in (a). (c) A typical SEM image of dimple structures formed on the fracture surface of Nb with oxygen charging at 500 °C. (d) A typical SEM image of semi-cleavage fracture surface of Nb with oxygen charging at 800 °C. With the increasing of oxygen charging temperature, the oxygen concentration will be enhanced in Nb. The tensile tests show that the strain hardening rate also increases with the elevating of oxygen concentration in Nb.

Figure S2

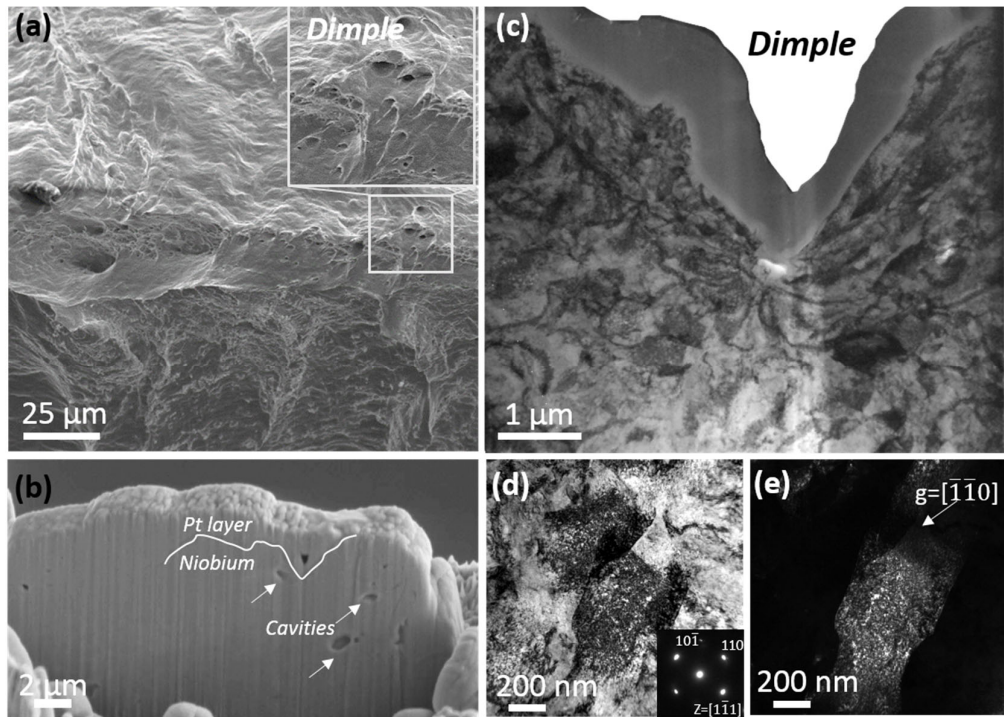


Fig. S2. Ductile fracture surface of Nb after bulk tensile test. (a) A typical SEM image of dimples on the fracture surface of Nb. (b) A typical SEM image of voids formed beneath the fracture surface which is taken during sample lifting process. The white line indicates the interface between the Pt coating (used as protecting ion damage during the lift-out) and the Nb. (c) A low magnification bright field TEM image of the microstructure beneath a dimple formed on the fracture surface. (d) and (e), typical bright field image and corresponding dark field image of dislocation microstructures found beneath the dimple in (c). The zone axis is $[1\bar{1}1]$.

Figure S3

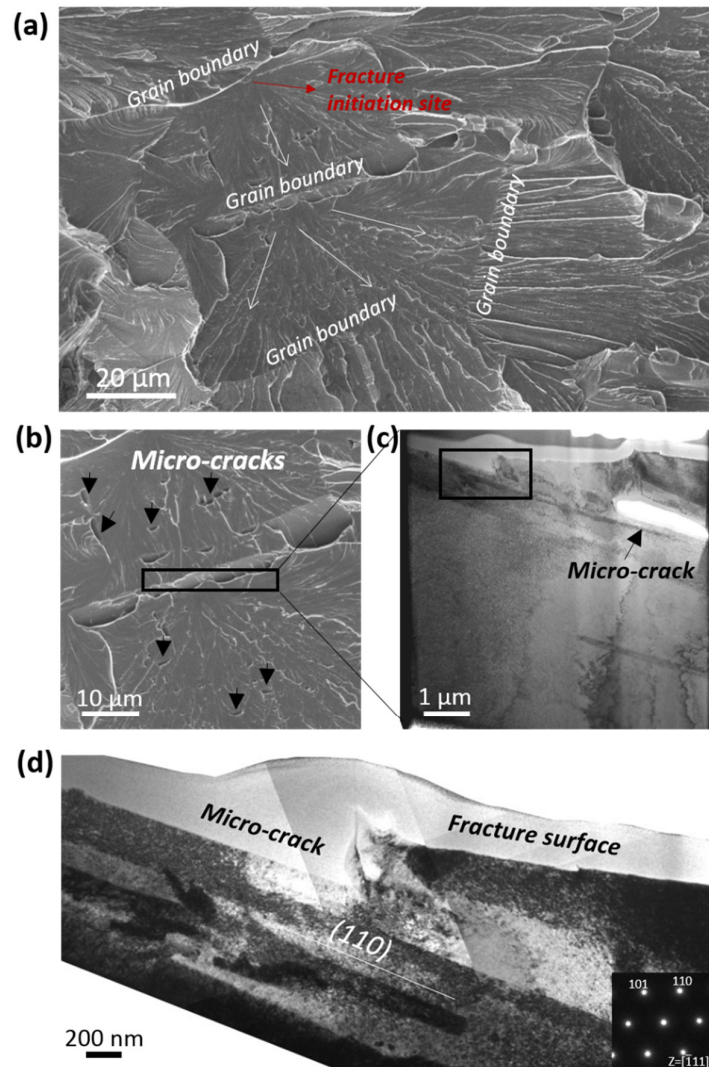


Fig. S3. Micro-cracks formed at fracture surface during bulk tensile test and microstructure beneath the large micro-crack. (a) A low magnification SEM image of fracture surface showing that the quasi-cleavage crack initiates at grain boundaries due to stress concentration. The white arrows indicate the propagation direction of quasi-cleavage crack. (b) A typical SEM image of micro-cracks at fracture surface in (a). The area within the black box is the position for TEM characterization using sample lifting technique. (c) A low magnification bright field TEM image of microstructure beneath fracture surface indicated by black box in (b). An obvious micro-crack beneath fracture surface can be observed. (d) A high magnification bright field TEM image of slip localization along (110) plane beneath large micro-crack of fracture surface.

Figure S4

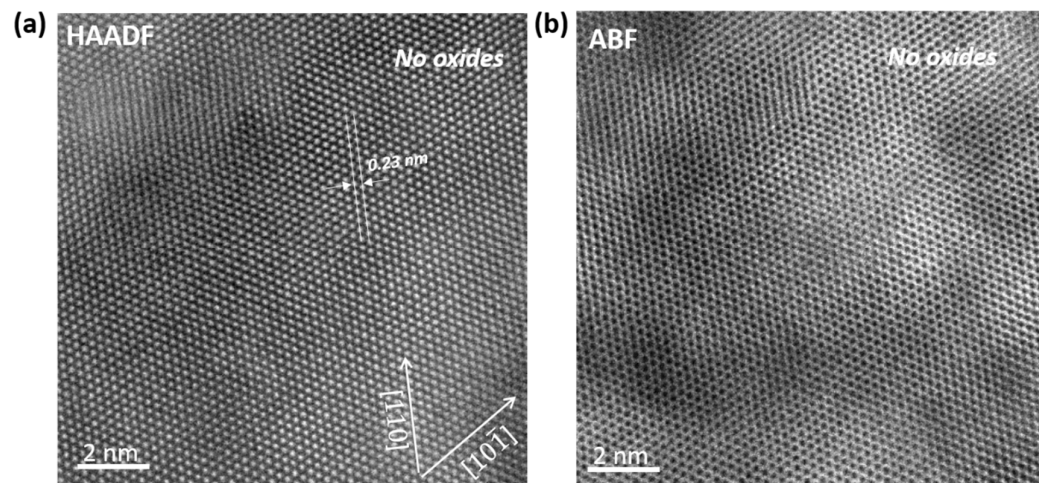


Fig. S4. The HRTEM image of localized slip band of Nb-O. (a) The High-Angle Annular Dark Field (HAADF) STEM image and (b) corresponding Annular Bright Field (ABF) image of localized slip band of Nb-O in Fig. 1(g). No oxides can be observed through the whole sample under high resolution TEM. The zone axis is $[1\bar{1}1]$. It should be noted that oxygen concentration with only ~ 1 at% in niobium is too low to be detected via the Z-contrast of the image.

Figure S5

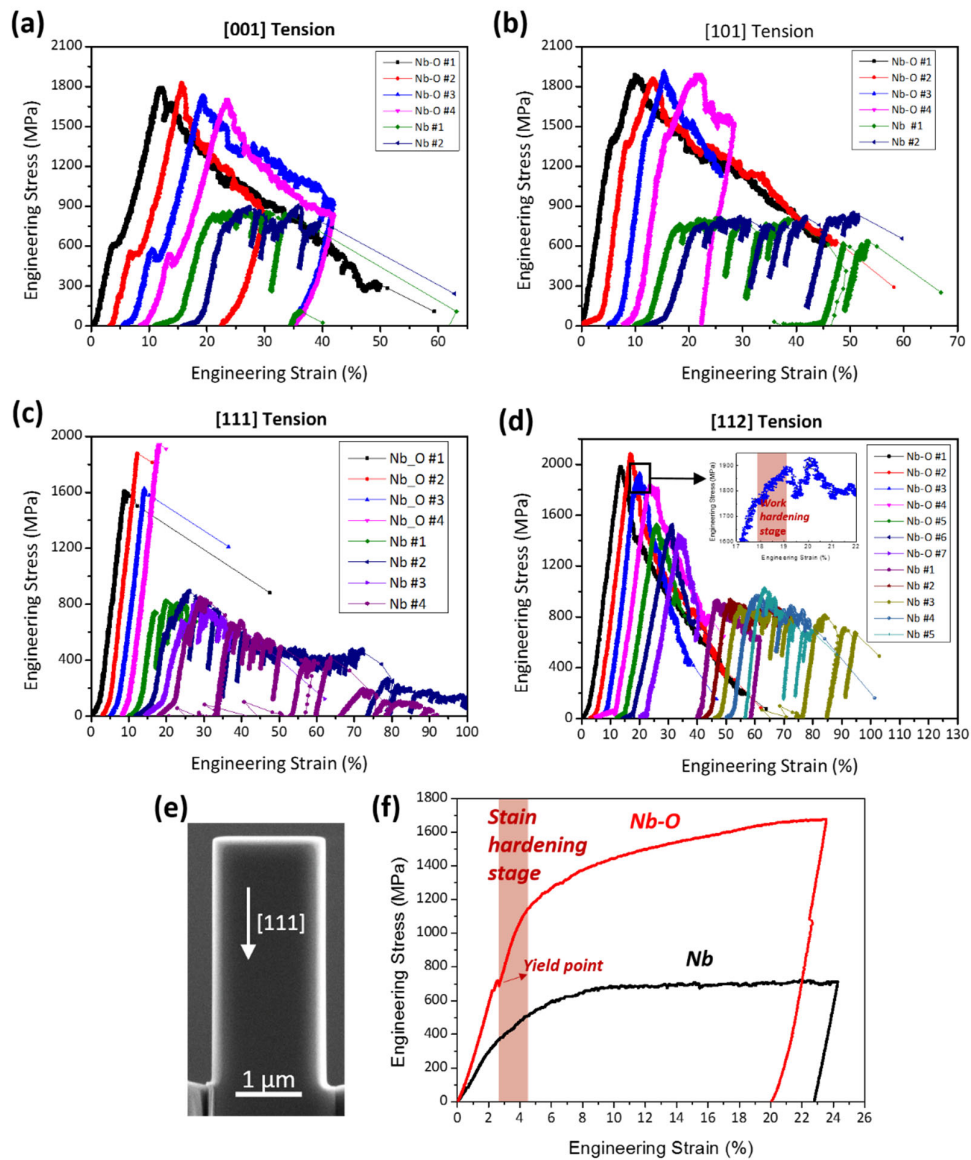


Fig. S5. Comparison for stress-strain curves of Nb and Nb-O submicron samples with different orientations. (a) [001] orientation. (b) [101] orientation. (c) [111] orientation and (d) [112] orientation, inset is the local enlarged view of a Nb-O curve showing strain hardening stage, and the strain hardening stage is very short in all [112] samples. (e) A SEM image of a square Nb-O pillar with [111] orientation. (f) The compression stress-strain curve of Nb and Nb-O along [111] orientation. The sample designations in (a-d) represent the repeats of the tensile test curves of the corresponding orientation. The compression test of [111] Nb-O demonstrate obvious strain hardening stage, as marked in the figure. The strong strain hardening is a common feature in Nb-O single crystals with different orientations.

Figure S6

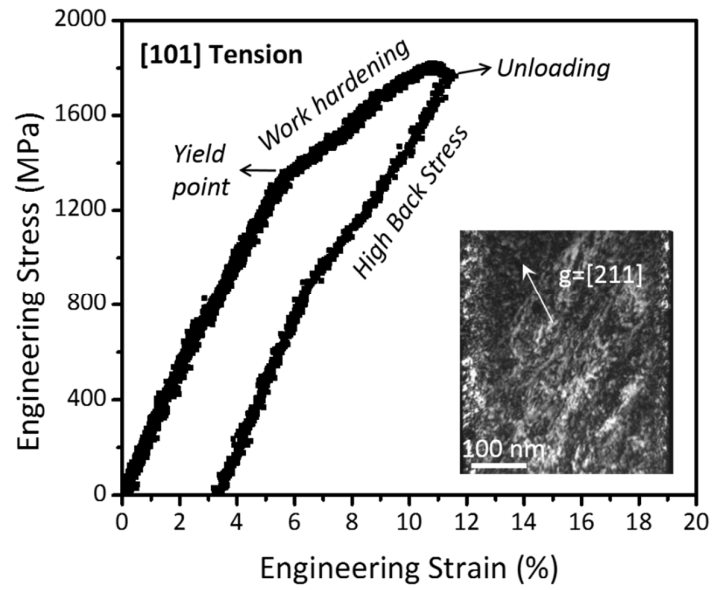


Fig. S6. Engineering stress-strain curve of [101] oriented Nb-O unloaded at $\sim 5\%$ plastic strain (interrupted in the strain hardening stage). The inset is the dark field TEM image of the dislocation structures formed after unloading (mainly screw dislocations). The unloading curve demonstrates an obvious elastic recovery stage indicating a high back stress accumulated during tensile loading, which indicates the strong interaction between dislocations and the dynamically formed obstacles.

Figure S7

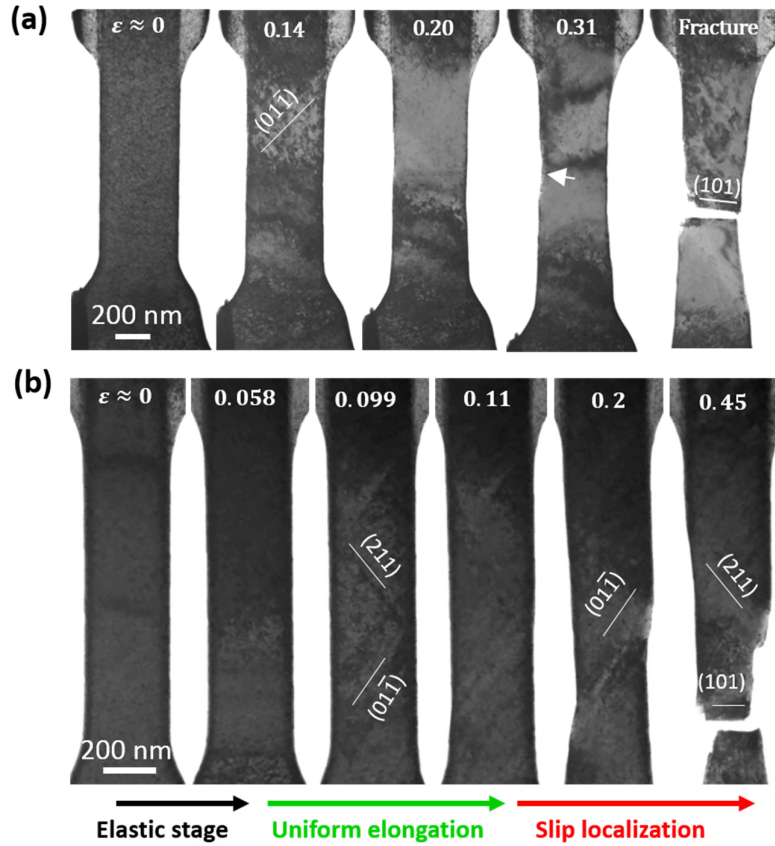


Fig. S7. Deformation process of [101] oriented submicron samples. (a) Pure Nb sample. The zone axis is $[\bar{1}11]$. Slip system along $(01\bar{1})$ plane is activated at $\sim 14\%$ strain. Mechanical annealing during tensile test of a [101] oriented pure Nb submicron sample was observed at $\epsilon \approx 0.2$, indicating weak ability in dislocation storage. Slip induced surface steps ($\sim 31\%$ strain indicated by white arrow) can also be observed. (b) Nb-O sample. Slip systems along (211) and $(01\bar{1})$ slip planes were both activated during the uniform deformation stage, while the following slip localization is mainly along the $(01\bar{1})$ slip planes and partially along (211) plane. Both samples show similar final fracture in terms of quasi-brittle separation along the (101) plane due to the low surface energy.

Figure S8

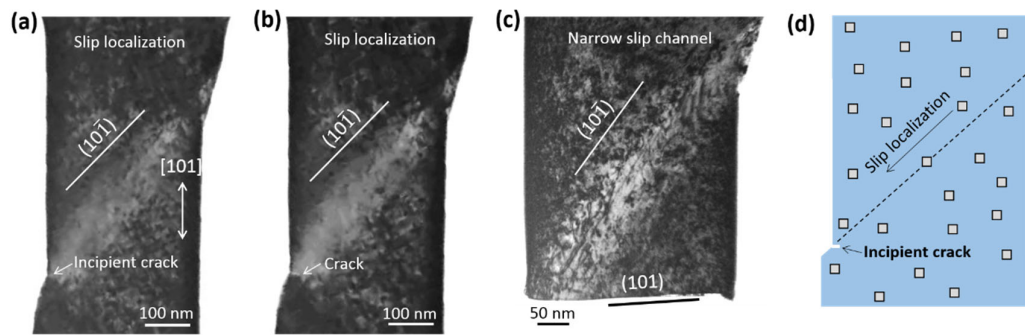


Fig. S8. Slip localization and fracture mechanism of submicron-sized Nb-O with $[101]$ orientations. (a) Slip localization in $[101]$ Nb-O induces surface slip step. (b) $[101]$ Nb-O with incipient crack nucleation at the sample edge. (c) A bright field TEM image of the cleavage fracture morphology of $[101]$ Nb-O and the narrow slip channel formed due to slip localization. (d) Schematic illustration of the slip localization induced incipient crack nucleation at the sample edge for $[101]$ Nb. (a), (b) and (c) are snapshots from continuous video tapping, with a time interval of 0.16 s.

Figure S9

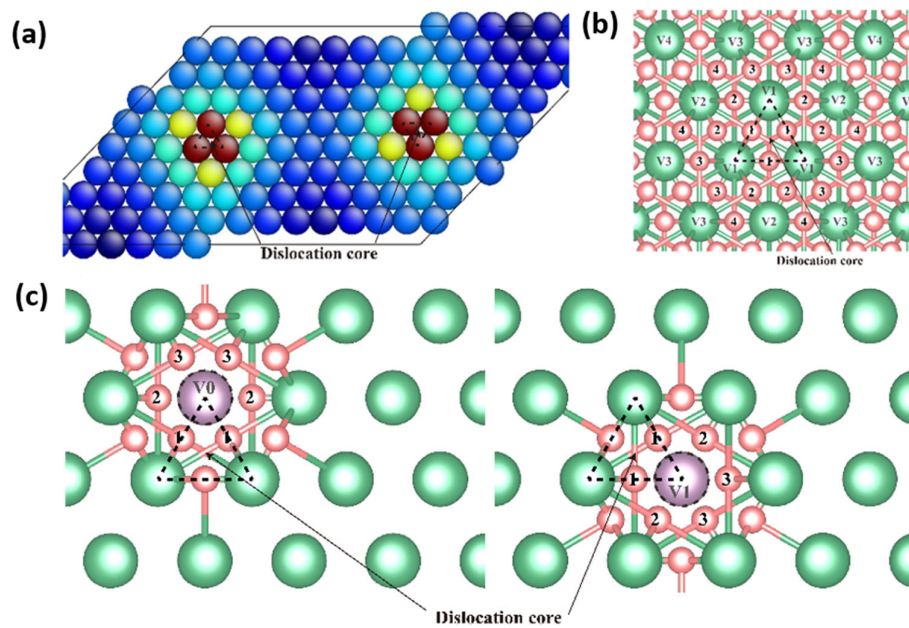


Fig. S9. Configurational relationship among SD, V and O. (a) Dislocation quadrupoles in a periodic cell. (b) 1st to 4th nearest neighbor V and O sites from dislocation core. (c) Relative configuration for three-body interactions.

Figure S10

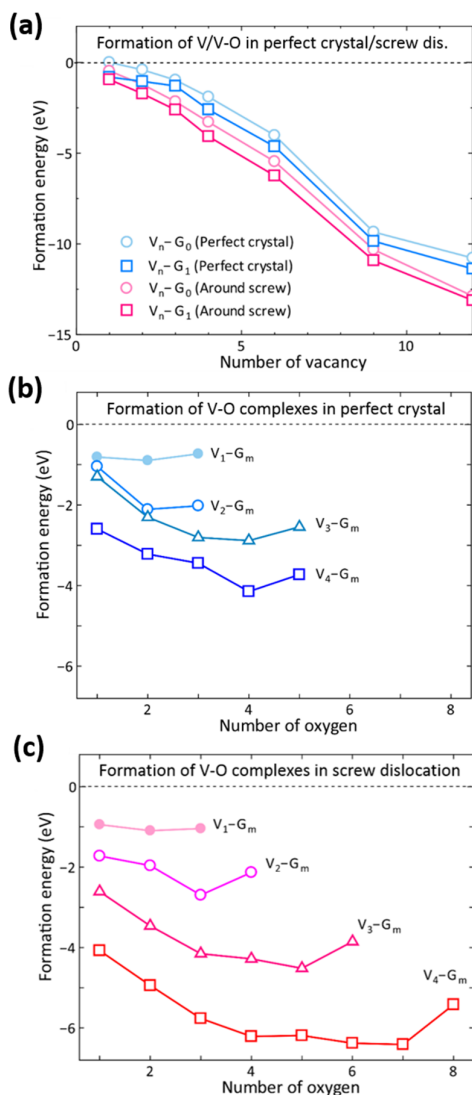


Fig. S10. Atomic calculation the formation energy of vacancy cluster and V-O complexes in perfect crystal or around a screw dislocation in Nb. (a) The formation energy of vacancy cluster will be reduced with adding oxygen atom or nucleating on screw dislocation in Nb. (b) With increasing the number of oxygen atoms, the formation energy of V-O complexes continually decrease. (c) The formation energy of V-O complexes will be reduced significantly when they are nucleated on screw dislocation. These results demonstrate that the three body interactions between vacancies, oxygen atoms and screw dislocation promote the formation of oxygen stabilized nano-cavities in Nb. G here is standing for gas atom and specifically for oxygen atom in this study.

Figure S11

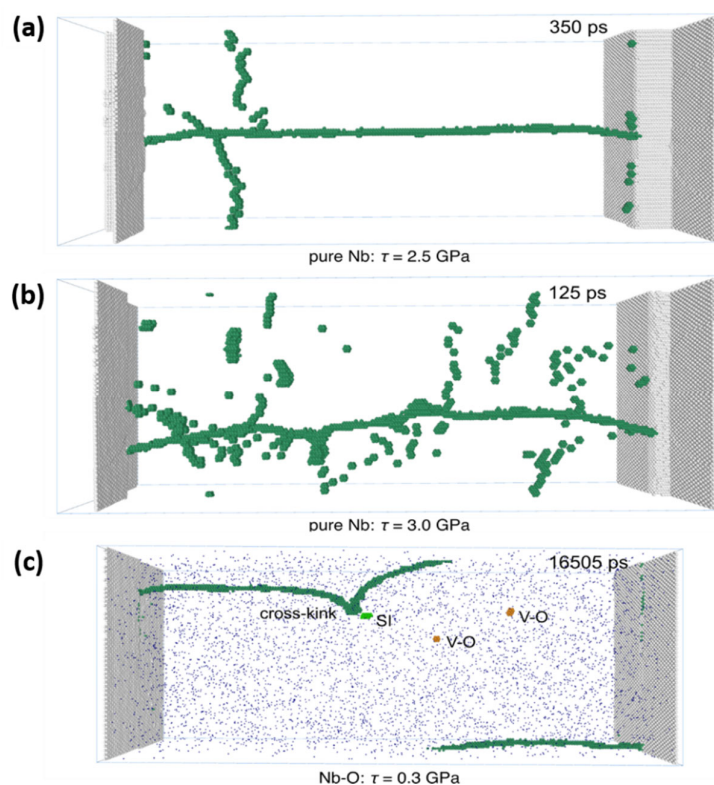


Fig. S11. Molecular dynamic simulation of screw dislocation movement and defect production in Nb and Nb-O subjected to constant shear stresses at 300 K. (a) Pure Nb sample under a shear stress of 2.5 GPa which is the critical shear stress to generate point defect. (b) Pure Nb sample under a shear stress of 3.0 GPa. (c) Nb-O sample (0.5 at% O) under a much lower shear stress of 0.3 GPa. Point defects can still be formed at this low stress level. Using another published Nb potential (*M.R. Fellinger, H. Park, J.W. Wilkins, Force-matched embedded-atom method potential for niobium, Phys. Rev. B 81 (2010) 114119.*), we also found a similarly high critical stress of 2.3 GPa to generate point defects.

Figure S12

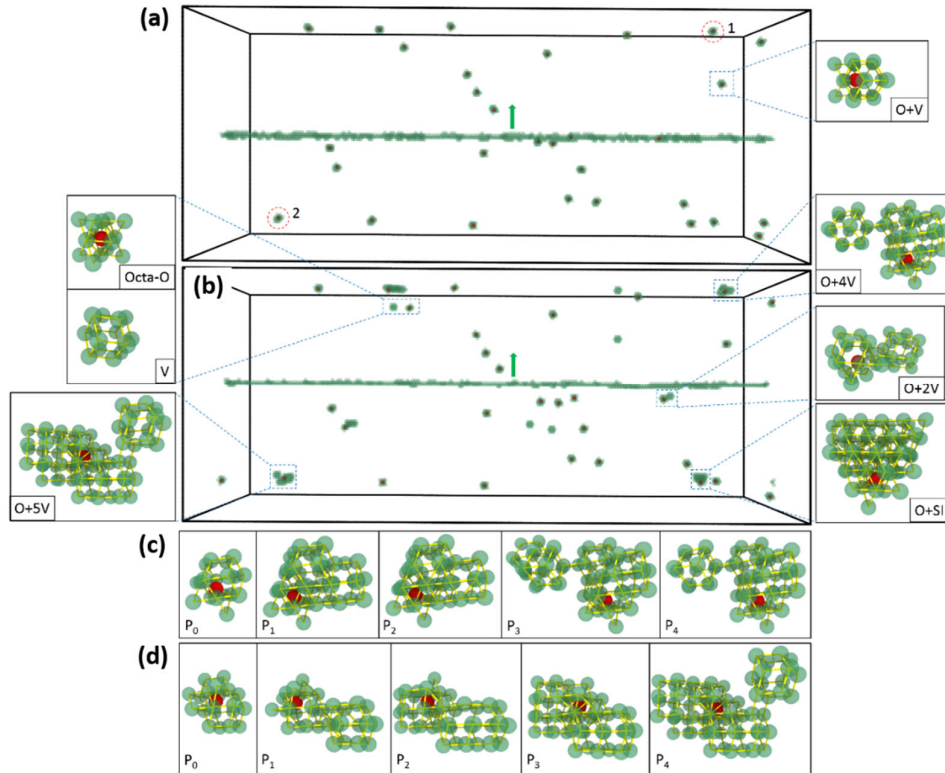


Fig. S12. Multiple passes of screw dislocation through VO complexes. (a) Atomic configuration at $t = 0$ ns or zero passage of the screw dislocation. (b) Atomic configuration at $t = 13.5$ ns or after four passes of the screw dislocation. Local defect clusters in both (a) and (b) are magnified for visualization. Oxygen generally resides on the octahedral interstitial site (Octa-O) and is simply denoted as O. V means vacancy and the number in front of V refers to the number of vacancies in the cluster. SI stands for self-interstitial. Arrows point to the direction of dislocation motion. (c) The evolving structures of VO complex 1 as circled in (a). (d) The evolving structures of VO complex 2 as circled in (a). P_1 , P_2 , P_3 and P_4 refer to the first, second, third and fourth passage of the screw dislocation, respectively. Some VO_1 complexes were found to grow into bigger VO_x ($x > 1$) clusters by absorbing vacancies from other VO_1 or from V-SI pairs generated by cross-kinking of screw dislocation. VO_x ($x > 1$) clusters exhibit relatively higher stability in resist to the sweep of the screw dislocation.

Figure S13

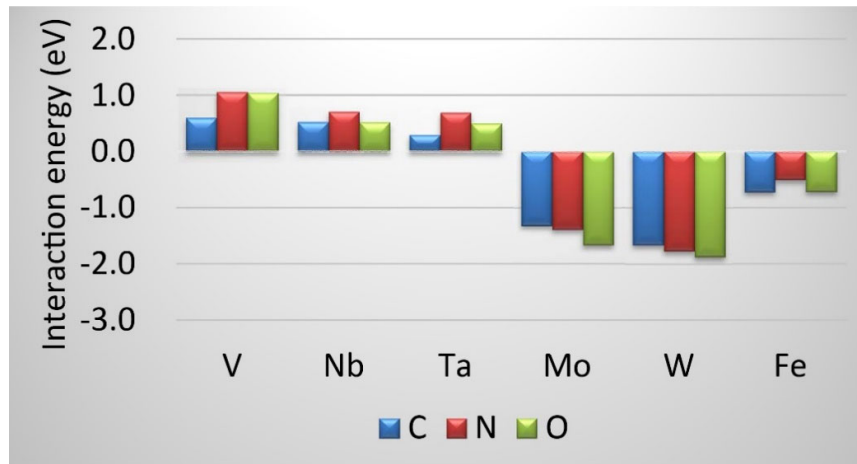


Fig. 13. The formation energy for hard core-interstitials composite. Carbon, nitrogen and oxygen interstitials were used for analysis. Interstitials are unstable around easy- and hard-core in Group V bcc metals, while interstitials become attractive at the center of hard-core in Group VI metals and Fe. More details about hard-core and easy-core can be found in Dezerald L. et al Physical Review B 89 (2014) 024104.

Movies

Movie S1: *In situ* TEM nanomechanical tensile testing of [101] submicron-sized Nb-O (speed up by 6 times).

Movie S2: *In situ* TEM nanomechanical tensile testing of [101] submicron-sized Nb-O, interrupted at 5% of plastic strain (speed up by 2 times).

Movie S3: *In situ* TEM nanomechanical tensile testing of [001] submicron-sized Nb with a sample thickness of 60 nm.

Movie S4: *In situ* TEM nanomechanical tensile testing of [001] submicron-sized Nb-O with a sample thickness of 60 nm.

Movie S5: Molecular dynamic simulation of the stability and evolution of V-O complexes under slip localization (cut by multiple screw dislocations).

Movie S6: Molecular dynamics simulation on a screw dislocation passing through 0.5 at.% O interstitials, forming many V-O complexes, vacancies, vacancy tubes. Green atoms are newly formed defects while grey atoms are the initial defects.

Movie S7: Molecular dynamics simulation on a screw dislocation passing through 1.0 at.% O interstitials, forming many V-O complexes, vacancies, vacancy tubes. Green atoms are newly formed defects while grey atoms are the initial defects.